

Novel constraints on fermionic dark matter from galactic observables II: galaxy scaling relations

C. R. Argüelles^{a,b}, A. Krut^{b,c,d}, J. A. Rueda^{b,c,e}, R. Ruffini^{b,c,e}

^a*Instituto de Astrofísica de La Plata (CCT La Plata, CONICET, UNLP), Paseo del Bosque, B1900FWA La Plata, Argentina*

^b*ICRANet, Piazza della Repubblica 10, I-65122 Pescara, Italy*

^c*Dipartimento di Fisica and ICRA, Sapienza Università di Roma, P.le Aldo Moro 5, I-00185 Rome, Italy*

^d*University of Nice-Sophia Antipolis, 28 Av. de Valrose, 06103 Nice Cedex 2, France*

^e*ICRANet-Rio, CBPF, Rua Dr. Xavier Sigaud 150, Rio de Janeiro, RJ, 22290-180, Brazil*

Abstract

We have recently introduced in paper I an extension of the Ruffini-Argüelles-Rueda (RAR) model for the distribution of DM in galaxies, by including for escape of particle effects. Being built upon self-gravitating fermions at finite temperatures, the RAR solutions develop a characteristic *dense quantum core-diluted halo* morphology which, for fermion masses in the range $mc^2 \approx 10 - 345$ keV, was shown to provide good fits to the Milky Way rotation curve. We study here for the first time the applicability of the extended RAR model to other structures from dwarfs to ellipticals to galaxy clusters, pointing out the relevant case of $mc^2 = 48$ keV. By making a full coverage of the remaining free parameters of the theory, and for each galactic structure, we present a complete family of astrophysical RAR profiles which satisfy realistic halo boundary conditions inferred from observations. Each family-set of RAR solutions predicts given windows of total halo masses and central quantum-core masses, the latter opening the interesting possibility to interpret them as alternatives either to intermediate-mass BHs (for dwarf galaxies), or to supermassive BHs (SMBHs, in the case of larger galaxy types). The model is shown to be in good agreement with different observationally inferred scaling relations such as: (1) the Ferrarese relation connecting DM halos with supermassive dark central objects; and (2) the nearly constant DM surface density of galaxies. Finally, the theory provides a natural mechanism for the formation of SMBHs of few $10^8 M_\odot$ via the gravitational collapse of unstable DM quantum-cores.

Keywords: Methods: numerical – Cosmology: dark matter – Galaxies: halos, nuclei, structure

1. Introduction

The problem of describing Dark Matter (DM) halos in terms of fundamental particles has gained considerable attention in the last years, given they may provide solutions to many of the unsuccessful predictions of the Cold Dark Matter (CDM) paradigm arising below ~ 10 kpc scales. The majority of such models are comprised within the following three different approaches: (i) The case of ultra light bosons with masses in the range $m_b c^2 \sim 1 - 100 \times 10^{-22}$ eV, known as ultra light DM, fuzzy DM (FDM) or scalar field DM (Baldeschi et al., 1983; Sin, 1994; Hu et al., 2000; Matos and Arturo Ureña-López, 2001; Robles and Matos, 2012; Hui et al., 2017; Bar et al., 2018); (ii) the case of Thomas-Fermi models based on fully-degenerate fermions with masses $m_{df} c^2 \sim \text{few } 10^2$ eV (Destri et al., 2013; Domcke and Urbano, 2015; Randall et al., 2017). We also include in this group similar models based on self-gravitating fermions but in the dilute regime (i.e.

Boltzmannian-like) which, however, *do not* imply an explicit particle mass dependence when contrasted with halo observables (see e.g. de Vega et al., 2014); (iii) the Ruffini-Argüelles-Rueda (RAR) model based on semi-degenerate configurations of self-gravitating fermions accounting for finite temperature and for relativistic effects, with masses in the range $m_f c^2 \sim \text{few } 10^1 - 10^2$ keV (Argüelles et al., 2013; Argüelles and Ruffini, 2014; Ruffini et al., 2015; Siutsou et al., 2015; Argüelles et al., 2016; Gómez et al., 2016; Argüelles et al., 2018).

One of the main interesting aspects of the above models is the particle mass dependence on their density profiles (besides the other physically-motivated free parameters), differently to the case of phenomenological profiles existing in the literature aiming to fit results from classical N-body numerical simulations. Moreover, such kind of self-gravitating systems of particles opens the possibility to have direct access to the nature, mass, and explicit phase-space distributions dependence at the onset of halo formation (see e.g., Hui et al., 2017 and refs. therein, for the case of bosons and, e.g. Argüelles et al., 2018 and refs. therein, for the case of fermions).

Email addresses: carlos.arguelles@icranet.org (C. R. Argüelles), andreas.krut@icranet.org (A. Krut), jorge.rueda@icra.it (J. A. Rueda), ruffini@icra.it (R. Ruffini)

However, not all of the above particle-motivated DM halo models have the required cosmological and astrophysical properties when contrasted with different observational data-sets. Some fundamental problems remain mainly within the cases (i) and (ii) such as: (a) galaxy-scaling relations; (b) Ly α forest constraints; (c) nearby disk galaxies with high resolution rotation curve features.

Concerning the first point (a), we could mention the recent results in [Deng et al. \(2018\)](#) which demonstrated that standard FDM models without self-interactions¹ are ruled out when asking to follow the DM-surface-density Universal relation ([Donato et al., 2009](#); [Rodrigues et al., 2017](#)). That is, while this observational relation imposes that the central DM halo density ρ_c scales with the inverse of the core radius r_c to some power $\beta \approx 1$ (i.e. $\rho_c \sim r_c^{-1}$); the FDM theory yields an inverse proportionality relation but with a quite different power $\beta_{\text{FDM}} = 4$.²

On a different observational ground, and moving to the issue (b), the DM particle mass constraints arising from recent Ly α forest observations, put severe bounds both to FDM particles (i), as well as to fermions (ii)-(iii). The key concept to understand how all such bounds arise is to recognize that the Ly α forest can be explained in terms of the standard cosmological model (see e.g. [Cen et al., 1994](#)), and therefore it can be directly linked to the matter power spectrum by offering a complementary probe for it ([Hui, 1999](#)). In the case of Warm Dark Matter (WDM) (exhibiting a linear matter power spectrum with a clear drop below a given threshold scale respect to the CDM paradigm), a lower bound of \sim few keV was found in [Viel et al. \(2013\)](#), see also [Yèche et al., 2017](#) for more general lower bounds above keV including for sterile neutrino WDM) from Ly α constraints. Such bounds are in strong tension with the below-keV Thomas-Fermi models cited above in (ii) as also discussed in [Randall et al. \(2017\)](#), while it remains in agreement with the RAR model introduced in (iii). Further discussion on FDM models regarding issues (b) and (c) will be given below in section 6.

We will show that the results of this work, together with the ones of the first article of this series ([Argüelles et al., 2018](#), hereafter Paper I) on the fit to the Milky Way full rotation curve, and the discussion of the constraints put to Λ CDM and Λ WDM cosmologies by the Ly α forest, favour instead the keV fermionic RAR model (iii).

In next section we introduce the main features of the RAR model (as originally given in Paper I). In section 3 we provide realistic halo boundary conditions as inferred from observational data coming from dwarf to elliptical galaxies. In section 4 we present the application of the extended RAR theory to different galaxy types as well as

galaxy clusters, and for fermion masses in the range limited by the Milky Way constraints. A more detailed description of the obtained families focusing on the configuration parameters is given in [Appendix A](#). We also briefly compare in [Appendix B](#) the applied method with an alternative set of constraints for dwarfs to verify its robustness.

In addition, we demonstrate in section 5 that the results of our model are consistent with (a) the observationally inferred correlations between the mass of the dark central object and total DM halo mass ([Ferrarese, 2002](#); [Kormendy and Bender, 2011](#); [Bogdán and Goulding, 2015](#)), and with (b) the observationally inferred (universal) value (within the $3 - \sigma$ error bars) of the inner surface density of DM halos ([Donato et al., 2009](#)), from dwarf to elliptical galaxies. Further *predicting* for possible deviations of a constant surface density (i.e. slight rising trend or positive tilt in a linear fit) towards the brightest objects, in striking similitude with the phenomenological results reported in [Boyarsky et al. \(2009\)](#).

Finally, in section 6 we summarize the conclusions of our results.

2. The RAR model

In Paper I ([Argüelles et al., 2018](#)) we have introduced an extension of the original RAR model ([Ruffini et al., 2015](#)), by considering a spherical system of self-gravitating fermions presenting a cutoff in the Fermi-Dirac phase-space distribution. Such a (coarse-grained) phase-space distribution can be obtained as a (quasi) stationary solution of a generalized Fokker-Planck equation for fermions (including the physics of violent relaxation and escape of particles), proper to deal with non-linear DM halo formation ([Chavanis, 2004](#)); which is written below:

$$f_c(\epsilon \leq \epsilon_c) = \frac{1 - e^{(\epsilon - \epsilon_c)/kT}}{e^{(\epsilon - \mu)/kT} + 1}, \quad f_c(\epsilon > \epsilon_c) = 0, \quad (1)$$

where $\epsilon = \sqrt{c^2 p^2 + m^2 c^4} - mc^2$ is the particle kinetic energy, μ is the chemical potential with the particle rest-energy subtracted off, T is the temperature, k is the Boltzmann constant, h is the Planck constant, c is the speed of light, and m is the fermion mass. We do not include the presence of anti-fermions, i.e. we consider temperatures $T \ll mc^2/k$. The full set of (functional) dimensionless-parameters of the model are defined by the temperature, degeneracy and cutoff parameters, $\beta = kT/(mc^2)$, $\theta = \mu/(kT)$ and $W = \epsilon_c/(kT)$, respectively.

The corresponding 4-parametric fermionic equation of state (at given radius r): $\rho(\beta, \theta, W, m)$, $P(\beta, \theta, W, m)$, is directly obtained as the corresponding integrals (bounded from above by $\epsilon \leq \epsilon_c$) over momentum space of $f_c(p)$, given in equations (1) and (2) in Paper I. Such components of the equation of state corresponds to the diagonal part of the stress-energy tensor in the Einstein equations, which are solved under the perfect fluid approximation within a background metric with spherical symmetry

¹ Composed, for example, by axion-like particles with $m_b c^2 \sim 10^{-22}$ eV as the one proposed in [Hu et al. \(2000\)](#); [Hui et al. \(2017\)](#).

² Alternative FDM models including for quartic-like self-interactions were also ruled out when contrasted against the above observed DM halo Universal-relation in [Deng et al. \(2018\)](#); see however [Robles and Matos \(2012\)](#) for other kind of self-interacting bosons.

$ds^2 = e^\nu c^2 dt^2 - e^\lambda dr^2 - r^2 d\Theta^2 - r^2 \sin^2 \Theta d\phi^2$ (with (r, Θ, ϕ) the spherical coordinates, and ν and λ only depending on the radial coordinate r). The system of Einstein equations is solved together with the Tolman and Klein thermodynamic equilibrium conditions, and (particle) energy conservation along a geodesic as given in equations 5, 6 and 7 of Paper I respectively. Finally, the dimensionless system of non-linear ordinary integro-differential equations reads:

$$\frac{d\hat{M}_{\text{DM}}}{d\hat{r}} = 4\pi\hat{r}^2\hat{\rho}, \quad (2)$$

$$\frac{d\theta}{d\hat{r}} = -\frac{1 - \beta_0(\theta - \theta_0)}{\beta_0} \frac{\hat{M}_{\text{DM}} + 4\pi\hat{P}\hat{r}^3}{\hat{r}^2(1 - 2\hat{M}_{\text{DM}}/\hat{r})}, \quad (3)$$

$$\frac{d\nu}{d\hat{r}} = \frac{2(\hat{M}_{\text{DM}} + 4\pi\hat{P}\hat{r}^3)}{\hat{r}^2(1 - 2\hat{M}_{\text{DM}}/\hat{r})}, \quad (4)$$

$$\beta(\hat{r}) = \beta_0 e^{\frac{\nu_0 - \nu(\hat{r})}{2}}, \quad (5)$$

$$W(\hat{r}) = W_0 + \theta(\hat{r}) - \theta_0. \quad (6)$$

Such that in the limit $W \rightarrow \infty$ (i.e. no particle escape: $\epsilon_c \rightarrow \infty$) these system reduce to the equations considered in the original RAR model (Ruffini et al., 2015). We have introduced the same dimensionless quantities as in the original RAR model formulation: $\hat{r} = r/\chi$, $\hat{M}_{\text{DM}} = GM_{\text{DM}}/(c^2\chi)$, $\hat{\rho} = G\chi^2\rho/c^2$, $\hat{P} = G\chi^2P/c^4$, where $\chi = 2\pi^{3/2}(\hbar/mc)(m_p/m)$ and $m_p = \sqrt{\hbar c/G}$ the Planck mass. We note that the constants of the Tolman and Klein conditions are evaluated at the center $r = 0$, indicated with a subscript ‘0’.

The task of Paper I (for the Milky Way), was thus to solve the system (2–6), for given regular initial conditions at the center, [$M_{\text{DM}}(0) = 0, \theta(0) = \theta_0, \beta(0) = \beta_0, \nu(0) = 0, W(0) = W_0$], for different DM particle mass m , to find solutions consistent with well-constrained DM halo observables of the Galaxy (see also beginning of next section). One of the main features of the RAR solutions is the fact that they are solved at finite temperature for *positive* central degeneracies $\theta_0 > 0$ (instead of the known diluted Boltzmannian-like regime $\theta_0 < 0$), giving rise to a degenerate core at the center of the halo which always fulfill the quantum condition: $\lambda_B \gtrsim 3l_c$ (where $l_c \sim n_c^{-1/3}$ is the interparticle mean distance within the core (with n_c the core particle density) and $\lambda_B = h/(2\pi mkT_c)^{1/2}$ the thermal de-Broglie wavelength at the core). The dense and degenerate core is followed by a transition from positive to negative values of θ where quantum corrections are still important, finally reaching the region of highly negative values corresponding to a Boltzmannian diluted regime (see fig. (2) in Paper I). Such a core-halo transition with the different physical behaviours in θ is easily understood by the fact that the fermions are immerse in an external gravitational field, leading to a radial gradient (monotonically decreasing) of the degeneracy.

This core-halo behaviour in the intrinsic RAR model parameters is reflected in the DM density and rotation curve profiles as follows (whose solution for the Milky Way

DM halo is displayed in figs. (3) and (4) in Paper I, for different RAR model paramters):

1. an inner core with radius r_c of almost constant density governed by quantum degeneracy (see the region of high positive values of the degeneracy parameter in upper panel of fig. 2 of Paper I);
2. an intermediate region with a sharply decreasing density distribution followed by an extended plateau, where quantum corrections are still important (see the region of transition from positive to negative values of degeneracy in upper panel of fig. 2 of Paper I); and
3. a Boltzmannian density tail (see highly negative values of the degeneracy parameter in upper panel of fig. 2 in Paper I) showing a behavior $\rho \propto r^{-n}$ with $n > 2$ due to the cutoff constraint (when W_0 approaches 0), as can be seen from lower panel of fig. 2 in Paper I.

3. Observational constraints

In the case of our Galaxy, thanks to the vast amount of rotation curve data, i.e. as obtained in Sofue, 2013, from inner bulge to outer halo, we were able to identify three relevant *observables* as the boundary conditions to be imposed to the RAR system of differential equations (2–6): a dark core mass $M_{\text{DM}}(r = r_c) \equiv M_c = 4.2 \times 10^6 M_\odot$ (alternative to the central BH) and two well constrained dark halo masses: $M_{\text{DM}}(r = 12 \text{ kpc}) = 5 \times 10^{10} M_\odot$; $M_{\text{DM}}(r = 40 \text{ kpc}) = 2 \times 10^{11} M_\odot$ (see Paper I: Argüelles et al., 2018). With such three observationally well constrained mass values for the Milky Way it was possible to obtain in Paper I the three (free) RAR model parameters (β_0, θ_0, W_0) for different particle masses m in the keV range.

It is now natural to ask whether or not the RAR model can explain the observational properties of other types of galaxies or even galaxy clusters, in the same range of DM particle mass obtained from the Milky way analysis. We therefore proceed to show how, for a fixed particle mass m , our model leads to an extensive three-parametric (θ_0, β_0, W_0) family of dark halos with parameters ranging from the ones of dwarf, to the ones in elliptical galaxies extending until galaxy clusters, harboring at the same time a semi-degenerate quantum core at each center.

When dealing with different galactic structures, located far away from us, the observational inferences of the DM content are limited to a narrow window of galaxy radii, usually lying just above the baryonic dominance region (i.e. typically up to several half-light radii). Generally, there is no observational access neither for the possible detection of a dark compact object at the centre nor for constraining the boundary of the DM halo at the virial radius scale. This is contrary to the case of the Milky Way, thus requiring a different phenomenology which is described in next.

We adopt here a similar methodology compared to the Milky Way analysis (Argüelles et al., 2018), but limited to

radial halo extents where observational data is available, allowing to constraint the DM halo mass either in a model independent (or dependent) manner. In particular we will select as the only boundary conditions taken from observables a characteristic halo radius r_h with the corresponding halo mass $M_h \equiv M_{\text{DM}}(r_h)$. The halo radius is defined as the location of the maximum of the halo rotation curve which we adopt as the one-halo scale length of our model. Thus, we define in next the parameters adopted for the different DM halos as constrained from observations in typical dwarf spheroidal (dSph), spiral, elliptical to galaxy cluster structures.

3.1. Typical dSph galaxies

We consider the eight best resolved dwarf satellites of the Milky Way as analyzed in Walker et al. (2009) by solving the Jeans equations, using large (stellar) kinematic data sets and including for orbital anisotropy.

There, it was reported a DM model-independent evidence of a maximum circular velocity (v_{max}) in the DM halo of the Fornax dwarf (see fig. 2 in Walker et al., 2009). Such an evidence was found by comparing the theoretical projected dispersion velocity (from Jeans equation) with the observed one (through a Markov-Chain Monte-Carlo method), using a 4-parametric generalized Hernquist mass model for the halo, the latter allowing either for cored or cuspy density profiles depending on the free parameters. The best fit to v_{max} was found independently of the couple of free parameters which control the DM shapes, i.e. in a DM independent way.

In the other seven cases, a DM model-dependent evidence for a circular velocity peak was found assuming either cuspy (e.g. NFW) or cored (e.g. cored-Hernquist) DM halos density profiles.

In all eight cases the inferred radii and masses at the maximum circular velocity (supported by data) are $r_{\text{max(d)}} \sim \text{few } 10^2 \text{ pc}$ and $M(r_{\text{max(d)}}) \sim \text{few } 10^7 M_{\odot}$. These values have been obtained by assuming a cored-Hernquist DM profile,³ similar to the RAR profiles here presented (see e.g. Ruffini et al., 2015; Argüelles et al., 2016 for the RAR halo fits to isothermal and Burkert profiles respectively).

The radius of maximal circular velocity we identify as the one-halo length scale of the RAR model $r_{h(d)} \equiv r_{\text{max(d)}}$ with the corresponding DM halo mass $M_{h(d)} \equiv M(r_{\text{max(d)}})$. Thus, as allowed by data, we adopt throughout this work the following fiducial values for the characteristic DM halo properties for typical dSphs:

$$r_{h(d)} = 400 \text{ pc} \quad (7)$$

$$M_{h(d)} = 3 \times 10^7 M_{\odot} \quad (8)$$

³ Somewhat larger values $r_{\text{max(d)}} \sim 1 \text{ kpc}$ and $M(r_{\text{max(d)}}) \sim 10^8 M_{\odot}$ are obtained for cuspy profiles. Though, the latter are disfavored respect to cored ones for dSph, as recently reviewed in Bullock and Boylan-Kolchin (2017).

3.2. Typical spiral galaxies

We consider some nearby disk galaxies observed in high resolution from the THINGS data sample (de Blok et al., 2008), where DM model-independent evidence for a maximum in the halo rotation curves is provided. Such an evidence is obtained by accounting for baryonic (stars and gas) components — thanks to the inclusion of infrared data from the *Spitzer* telescope — in addition to the (total) observed rotation curve from the HI tracers. They calculated along the full observed data coverage, the DM contribution v_{halo} to the observed rotation curve v_{obs} , by means of $v_{\text{halo}}^2 = v_{\text{obs}}^2 - v_{\text{bar}}^2$, through the corresponding build up of mass models for the baryonic components $v_{\text{bar}}^2 = \Upsilon_* v_*^2 + v_{\text{gas}}^2$ (with Υ_* the stellar mass-to-light ratio).

This analysis shows galaxies with extended enough data coverage (mainly corresponding to the larger and more luminous) supporting for evidence of a maximum in the circular velocity (see gray curves within fig. 63 in de Blok et al., 2008). The maximum values for radii and velocity in the more luminous galaxies ($M_B \lesssim -20$) are expected to be bounded from above and below as, $r_{\text{max(s)}} \approx 10 - 80 \text{ kpc}$, and $v(r_{\text{max(s)}}) \approx 70 - 310 \text{ km/s}$, further implying $M(r_{\text{max(s)}}) \approx 10^{10} - 2 \times 10^{12} M_{\odot}$. The bounds for $r_{\text{max(s)}}$ and $v(r_{\text{max(s)}})$ are reported in de Blok et al. (2008, fig. 63) using NFW models with data supporting up to $\approx 50 \text{ kpc}$. Note the similar behaviour between the NFW and the RAR models on the halo scales of interest, as shown in Argüelles et al. (2018, fig. 3) for the case of the Milky Way.

Analogue to dwarf galaxies we identify the radius of the maximal circular velocity as the one-halo length scale $r_{h(s)} \equiv r_{\text{max(s)}}$ with the corresponding DM halo mass $M_{h(s)} \equiv M(r_{\text{max(s)}})$. Thus, as allowed by data, we adopt throughout this work the following fiducial values for the characteristic DM halo properties for typical spirals:

$$r_{h(s)} = 50 \text{ kpc} \quad (9)$$

$$M_{h(s)} = 1 \times 10^{12} M_{\odot} \quad (10)$$

3.3. Typical elliptical galaxies

We consider a sample of elliptical galaxies from Hoekstra et al. (2005), studied via weak lensing signals, and further analyzed in Donato et al. (2009) by providing halo mass models for the tangential shear of the distorted images (i.e. galaxies taken from Appendix A in Donato et al., 2009).

We also consider the iconic case of the largest and closest elliptical M87 as studied in Romanowsky and Kochanek (2001), accounting for combined halo mass tracers such as stars, Globular Clusters (GCs) and X-ray data (see also Nulsen and Bohringer, 1995).

Kinematic measurements (e.g. GCs) can probe distances up to several 10^1 kpc , while X-ray and weak lensing data can reach much further distances up to several 10^2 kpc . Thus, the latter usually allow for (DM model-dependent) evidence of a maximum circular velocity on halo scales, where data supports. Such an evidence was provided in Donato et al. (2009) and Romanowsky and Kochanek (2001)

through the DM profiles (i.e. Burkert and NFW respectively), to obtain best fits to the full data coverage in the galaxies there considered. Providing the following maxima values: $r_{\max(e)} \approx 100$ kpc and $M(r_{\max(e)}) \approx 10^{12} M_{\odot}$ (in the case of the more luminous ellipticals with $M_B < -20$, following Burkert) up to $\approx 10^{13} M_{\odot}$ (in the case of M87, following NFW).

Again, we identify here the radius of the maximal circular velocity as the one-halo length scale $r_{h(e)} \equiv r_{\max(e)}$ with the corresponding DM halo mass $M_{h(e)} \equiv M(r_{\max(e)})$. Thus, as allowed by data, we adopt throughout this work the following fiducial values for the characteristic DM halo properties for typical ellipticals:

$$r_{h(e)} = 90 \text{ kpc} \quad (11)$$

$$M_{h(e)} = 5 \times 10^{12} M_{\odot} \quad (12)$$

3.4. Typical galaxy clusters

We consider a sample of 7 brightest cluster galaxies (BCGs) from Newman et al. (2013). In that work the luminous and dark components were separated to obtain DM distributions which can be well described by a generalized NFW (gNFW) model (Zhao, 1996), developing a maximal velocity at the one-halo length scale $r_{\max(\text{bcg})}$. Such morphology is shown in Newman et al. (2013) to be supported by data sets including for weak lensing and stellar kinematics, covering a radial extend from 10 kpc up to 3 Mpc. In all cases the halo radii and masses can be inferred from such gNFW profiles and read $r_{\max(\text{bcg})} \approx 10^2 - 10^3$ kpc, and $M(r_{\max(\text{bcg})}) \approx 10^{14} - 10^{15} M_{\odot}$ respectively.

Equivalent to other galaxy types, we identify here the radius of the maximal circular velocity as the one-halo length scale $r_{h(\text{bcg})} \equiv r_{\max(\text{bcg})}$ with the corresponding DM halo mass $M_{h(\text{bcg})} \equiv M(r_{\max(\text{bcg})})$. For simplicity we take the mean values of the inferred radii and masses as typical values for BCGs. Thus, as allowed by data, we adopt throughout this work the following fiducial values for the characteristic DM halo properties for typical BCGs:

$$r_{h(\text{bcg})} = 600 \text{ kpc} \quad (13)$$

$$M_{h(\text{bcg})} = 3 \times 10^{14} M_{\odot} \quad (14)$$

3.5. Method

The halo values adopted above for each (representative) galaxy or BCG, are such that

- they correspond to DM dominated halos as carefully checked in each observational work cited above;
- they do not account for the (total) virial DM mass due to natural observational limitations, but they rather represent the DM halo characteristics somewhat outside the region of baryon dominance.

We thus systematically calculate (for the relevant example of $mc^2 = 48$ keV as motivated by the Milky Way analysis in Paper I) the RAR solutions represented through

the configuration parameter (β_0, θ_0, W_0) , which match the halo constraints r_h and M_h with a tolerance $\tau = 10^{-3}$ under the least-square condition

$$\sum_{i=1}^N \left| 1 - \frac{f_i^{\text{RAR}}(\mathbf{b})}{y_i} \right|^2 < \tau^2. \quad (15)$$

Here, the observables y_i for each galaxy or BCG case are compared with the predictions $f_i^{\text{RAR}}(\mathbf{b})$ for a parameter vector $\mathbf{b} = (\beta_0, \theta_0, W_0, m)$. The associated set of constraints (r_h, M_h) with $N = 2$ are given in eqs. (7) and (8) for dwarfs, eqs. (9) and (10) for spirals, eqs. (11) and (12) for ellipticals and eqs. (13) and (14) for BCGs.

Notice that the observational constraints necessarily imply astrophysical RAR solutions which develop a maximum in the halo rotation curve (i.e. as set by r_h). Additionally, we request to the solutions one extra (underlying) physical condition, hereafter the *quantum core* condition: the compact-core is stable or non-critical (i.e. it does not have the critical mass of gravitational collapse to a BH), fulfilling the quantum-statistics relation $\lambda_B \gtrsim 3l_c$ in the core. These conditions define the full window of astrophysically allowed RAR-family solutions. Importantly, the two halo constraints (for given m) provide a one-parametric family within the full ranges of the three configuration parameters $(\beta_0, \theta_0, \text{and } W_0)$. Thus, the obtained values lay along a one-dimensional curve in the free configuration space and are limited from below and above; see Appendix A for further details.

4. Results

The RAR model provides, for each galaxy type and BCG with given *observables* (r_h, M_h) , a continuous set of solutions which is illustrated as a blue shaded region in fig. 1. In particular, we show five benchmark solutions, labeled with their central densities (from black to magenta, roughly enveloping the blue shaded regions), for DM mass distributions $M_{\text{DM}}(r)$, rotation curves $v_{\text{DM}}(r)$ and density profiles $\rho(r)$. All solutions have been calculated for the relevant example of $mc^2 = 48$ keV, with corresponding full set of free RAR parameters as detailed in Appendix A.

They encompass a window of possible core and total masses, labeled as M_c and M_{tot} , for each galactic structure (see table 1 for benchmark numerical values and fig. A.7 for full range). Importantly, those mass windows are bounded from above and below as dictated by the astrophysical (i.e. v_{max} at r_h) and *quantum core* conditions (see Appendix A for details).

The core mass $M_c \equiv M_{\text{DM}}(r_c)$ is given at the core radius, defined at the first maximum of the rotation curve (analogously to the halo radius definition). The outermost DM halo mass $M_{\text{tot}} \equiv M_{\text{DM}}(r_b)$ is obtained at the border radius r_b , which is defined by $\rho(r_b) = 0$, above which there is no remaining particle energy as set by the RAR cutoff parameter condition $W(r_b) = 0$ (see section 2). Both masses are an outcome of the RAR family of astrophysical

DWARFS								
$M_h = 3 \times 10^7 M_\odot, r_h = 400 \text{ pc}$								
ρ_0	β_0	θ_0	W_0	M_c	r_c	M_{tot}	r_b	ρ_{pl}
M_\odot/pc^3				M_\odot	pc	M_\odot	pc	M_\odot/pc^3
1.1×10^{10}	1.4×10^{-9}	23.8	∞	3.9×10^3 (§)	6.3×10^{-3}	∞	∞	1.2×10^0
5.3×10^{11}	1.8×10^{-8}	24.5	43.9	2.7×10^4	3.3×10^{-3}	3.9×10^7	8.2×10^2	4.4×10^{-1}
2.3×10^{13}	2.6×10^{-7}	21.1	37.7	1.8×10^5	1.8×10^{-3}	3.9×10^7	8.1×10^2	4.5×10^{-1}
8.9×10^{14}	3.6×10^{-6}	17.7	31.8	1.1×10^6	9.6×10^{-4}	4.0×10^7	8.7×10^2	4.4×10^{-1}
3.5×10^{16}	4.5×10^{-5}	16.1	29.3	7.0×10^6 (†)	5.2×10^{-4}	6.4×10^7	1.7×10^3	4.1×10^{-2}
SPIRALS								
$M_h = 1 \times 10^{12} M_\odot, r_h = 50 \text{ kpc}$								
1.1×10^{14}	4.0×10^{-7}	40.9	∞	3.9×10^5 (§)	1.3×10^{-3}	∞	∞	2.4×10^{-2}
5.8×10^{15}	5.4×10^{-6}	41.6	73.2	2.8×10^6	6.9×10^{-4}	1.3×10^{12}	9.8×10^4	8.3×10^{-3}
2.2×10^{17}	6.5×10^{-5}	38.5	67.6	1.7×10^7	3.8×10^{-4}	1.3×10^{12}	9.6×10^4	8.2×10^{-3}
9.3×10^{18}	8.3×10^{-4}	35.8	62.3	9.7×10^7	1.9×10^{-4}	1.3×10^{12}	9.6×10^4	8.2×10^{-3}
3.3×10^{20}	6.7×10^{-3}	39.6	64.4	2.2×10^8 (*)	7.8×10^{-5}	1.3×10^{12}	9.6×10^4	8.2×10^{-3}
ELLIPTICALS								
$M_h = 5 \times 10^{12} M_\odot, r_h = 90 \text{ kpc}$								
5.4×10^{14}	1.1×10^{-6}	43.3	∞	8.5×10^5 (§)	1.0×10^{-3}	∞	∞	1.8×10^{-2}
1.9×10^{16}	1.1×10^{-5}	44.3	77.9	5.1×10^6	5.7×10^{-4}	6.5×10^{12}	1.9×10^5	6.3×10^{-3}
5.2×10^{17}	1.1×10^{-4}	41.6	72.9	2.6×10^7	3.3×10^{-4}	6.4×10^{12}	1.8×10^5	6.2×10^{-3}
1.5×10^{19}	1.0×10^{-3}	39.7	68.7	1.2×10^8	1.7×10^{-4}	6.4×10^{12}	1.8×10^5	6.2×10^{-3}
4.3×10^{20}	6.7×10^{-3}	45.5	73.0	2.2×10^8 (*)	7.2×10^{-5}	6.4×10^{12}	1.8×10^5	6.2×10^{-3}
BCGs								
$M_h = 3 \times 10^{14} M_\odot, r_h = 600 \text{ kpc}$								
1.8×10^{16}	9.5×10^{-6}	50.0	∞	4.9×10^6 (§)	5.7×10^{-4}	∞	∞	3.6×10^{-3}
2.5×10^{17}	5.3×10^{-5}	51.6	90.9	1.8×10^7	3.7×10^{-4}	4.0×10^{14}	1.3×10^6	1.3×10^{-3}
2.6×10^{18}	2.6×10^{-4}	50.3	87.9	5.6×10^7	2.4×10^{-4}	3.9×10^{14}	1.2×10^6	1.3×10^{-3}
2.8×10^{19}	1.2×10^{-3}	50.1	86.2	1.4×10^8	1.5×10^{-4}	3.9×10^{14}	1.2×10^6	1.2×10^{-3}
2.9×10^{20}	4.4×10^{-3}	55.7	90.7	2.2×10^8 (*)	8.2×10^{-5}	3.9×10^{14}	1.2×10^6	1.2×10^{-3}

(§) minimum quantum core mass for each galaxy type associated with the limited isothermal-like solutions
(†) maximum core mass for dwarfs corresponding to the solutions without maximum in the halo rotation curve
(*) critical core mass value M_c^{cr} just before reaching the gravitational collapse

Table 1: Free RAR model parameters for the 5 benchmark sets of DM profiles given in fig. 1, for the case of $mc^2 = 48 \text{ keV}$, together with the DM masses (M_c , M_{tot}) and radii (r_c , r_b), as well as central and plateau densities (ρ_0 , ρ_{pl}) for galactic structures from dwarfs to BCGs.

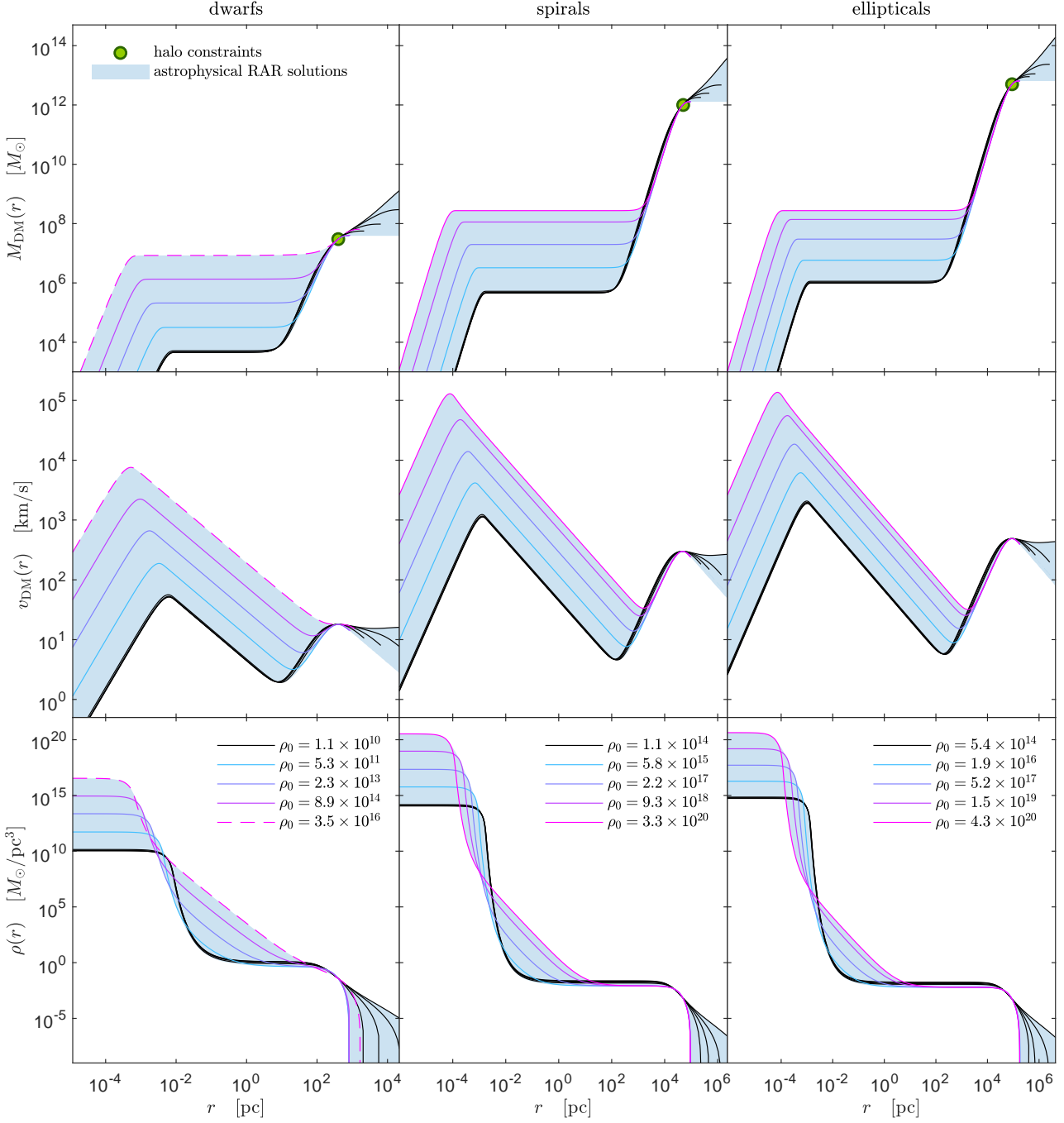


Figure 1: Astrophysical RAR solutions, for the relevant case of $mc^2 = 48 \text{ keV}$, fulfill observationally given DM halo restrictions (r_h, M_h) for typical dwarf (left), spiral (middle) and elliptical galaxies (right). Shown are density profiles (bottom), rotation curves (middle) and DM mass distributions (top). The full window for each galaxy type is illustrated by a blue shaded region and enveloped approx. by 5 benchmark solutions inside. Each solution is labeled with the central density in units of $M_\odot \text{pc}^{-3}$ (the reader is referred to [Appendix A](#) for the explicit relation with the free parameters of the theory). The continuous-magenta curves, occurring only for spiral and elliptical galaxies, indicates the critical solutions which develop compact critical cores (before collapsing to a BH) of $M_c^{\text{cr}} = 2.2 \times 10^8 M_\odot$. The dashed-magenta curves for dwarfs are limited (instead) by the astrophysical necessity of a maximum in the halo rotation curve. The bounding black solutions correspond to the ones having the minimum core mass (or minimum ρ_0) which in turn imply larger cutoff parameters (implying $\rho \propto r^{-2}$ when $W_0 \rightarrow \infty$).

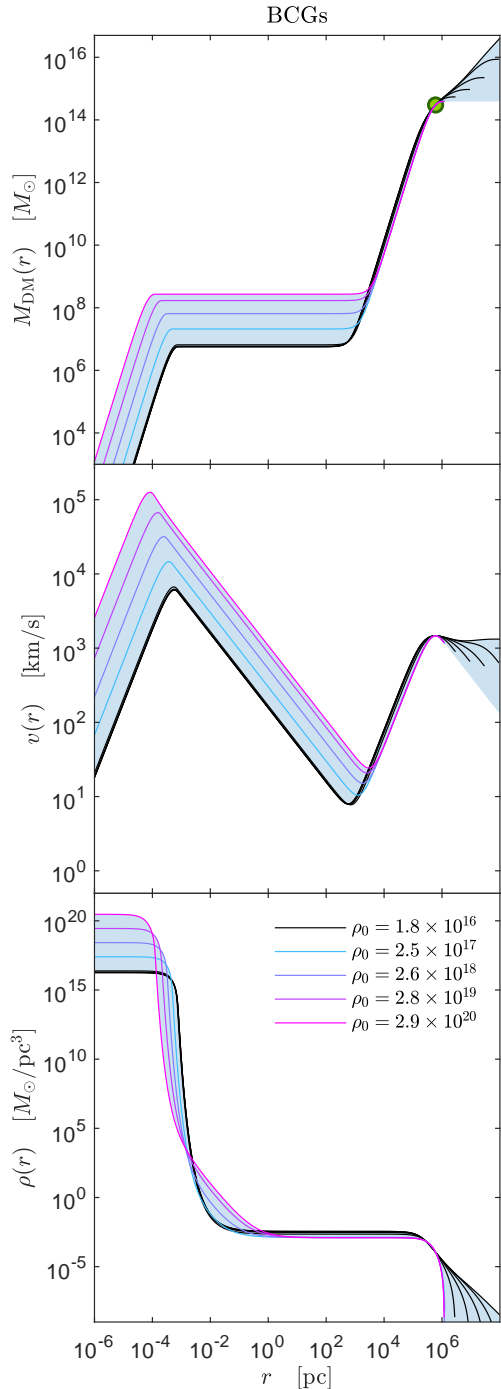


Figure 1 (cont.): Profiles of BCGs.

solutions and can be considered as a prediction of our theory (see table 1).

The critical solutions, reaching the limiting core mass $M_c^{\text{cr}} \approx 2.2 \times 10^8 M_\odot$ achieved only by the typical spiral and elliptical galaxies as well as for larger BCGs, are represented by the continuous magenta curves. The dashed magenta curve, in contrast, indicates the limiting (non-critical) solutions for typical dwarfs, where no maximum halo rotation curve is present (i.e. halo-scale v_{max} and

plateau-scale v_{min} merge to a saddle point in the rotation curve).

On the other hand, the black curves correspond to the solutions acquiring the lowest possible central density ρ_0 but with a cutoff affecting the outer halo tails. These solutions develop more and more extended density tails resembling isothermal-like solutions, corresponding to $\rho \propto r^{-2}$ at large radii. Accordingly, the limiting case $W_0 \rightarrow \infty$ resembles fully isothermal solutions, infinite in mass and size, in agreement with what was obtained in the original version of the model (Ruffini et al., 2015).

The astrophysical conditions imposed to the solutions put no limit on the maximum value of W_0 . Unless no other observational constraint is available (for a given galaxy) regarding the ending trend in the shape of the density tail, W_0 can increase indefinitely. Indeed, the larger W_0 the lesser the hardness in the falling-down shape of density profiles beyond r_h and the larger the boundary radius r_b . Of course, at some point r_b (and consequently M_{tot}) will be excessively large to represent any reliable astrophysical halo. Therefore, those RAR solutions must be discarded as physical ones (see section 5 for the usage of a quantitative condition). We show, for completeness, at bottom left of fig. 1 (black lines) the full plethora of density tails, corresponding with the specific minimum core mass solutions for each galaxy type.

It is important to make explicit that in all the cases analyzed the quantum core condition $\lambda_B \gtrsim 3l_c$ is fulfilled. We obtain $\lambda_B \gtrsim 2.7l_c$ for dSphs, $\lambda_B \gtrsim 3.6l_c$ for typical spirals, $\lambda_B \gtrsim 3.8l_c$ for normal elliptical galaxies and $\lambda_B \gtrsim 4l_c$ for typical BCGs.

In sum we find that dark halos from dSph all the way up to BCG can be explained with regular and continuous distributions of the same type of fermions, having a particle mass of $mc^2 \sim 50 \text{ keV}$. Instead of massive BHs at their centres, our solutions develop massive and compact quantum cores with masses in the range

- $M_c \approx 3.9 \times 10^3 - 7.0 \times 10^6 M_\odot$ for typical dSphs
- $M_c \approx 3.9 \times 10^5 - 2.2 \times 10^8 M_\odot$ for typical spirals
- $M_c \approx 8.5 \times 10^5 - 2.2 \times 10^8 M_\odot$ for typical ellipticals
- $M_c \approx 4.9 \times 10^6 - 2.2 \times 10^8 M_\odot$ for typical BCGs

The smaller the dark halos (from dSphs to typical ellipticals to typical BCGs), the lesser their masses and the lesser their core compactness, and viceversa. This tendency ends at the larger (i.e. more extended) DM halos, having a core of critical mass which is described in more detail by the continuous-magenta solutions (e.g. typical spirals, ellipticals and BCGs) in fig. 1. Additionally, the trend can be checked by comparing the group of values in columns 8 with 5 and 6 among the different galactic structures in table 1.

The quantum core masses M_c , the total halo masses M_{tot} and the (consequent) associated window for the plateau

densities ρ_{pl} (defined at the minimum of the RAR rotation curve and inherent to each of the RAR solutions), have to be considered as explicit predictions of the RAR model.⁴ These predicted values are contrasted in more details within the context of the $M_{\text{BH}} - M_{\text{tot}}$ relation and the constancy of the *central* surface DM density in section 5, as a consistency check of the model.

4.1. Galaxy fitting examples: the case of Sculptor and UGC05986

4.1.1. The Sculptor dSph

The aim is thus to link our typical RAR solutions for dSphs with a proper observable such as the (projected) dispersion velocity $\hat{\sigma}$ arising from Jeans analysis (as the one applied for dwarfs in Walker et al., 2009) to be then compared with the corresponding data. We will consider for definiteness one of the best resolved MW satellites such as the Sculptor galaxy, as studied in Walker et al., 2009. For this we assume our RAR DM mass profile $M_{\text{DM}}(r)$ and a Plummer profile for the stellar (surface) density (with the corresponding r_{half} and orbital anisotropy for stellar components adopted in Walker et al., 2009). This is done for the five different benchmark solutions ($mc^2 = 48 \text{ keV}$) as given in fig. 1. From this (back-of-the-envelope) comparison, which is shown in fig. 2, it turns out that while all of our solutions provide reasonable fits on halo scales⁵ (somewhat similar to the cored-halo profile assumed in Walker et al., 2009), some of them present a clear mismatch (of nearly a factor 2) through the more central inner-halo scales (see dashed-magenta curve in fig. 2). This clear difference occurs for the solutions with central temperatures close to β_0^{max} , i.e. the ones having exceedingly large Keplerian velocity cores reaching inner halo scales of few $\sim 10 \text{ pc}$.

It is important to further emphasize that such $\hat{\sigma}$ data mismatch through the center, is only present for the RAR solutions developing a cuspy trend in $\rho(r)$, which in turn occurs only for the larger β_0 solutions. Interestingly, such trend arises because of the much small extension of dSphs respect to the larger galaxy types together with the astrophysical condition (presence of a maximum in the halo rotation curve) imposed to the solutions. Indeed, when such condition is no longer fulfilled (see saddle-point behaviour in $v(r)$ for dSphs in dashed-magenta in fig. 1), an unphysical fast rising trend in $\hat{\sigma}$ arises, evidencing the relevance of asking for such astrophysical condition in the rotation curve.

⁴ The reader is referred to Appendix A for a full description of the limiting predicted properties of the RAR profiles in terms of the free model parameters.

⁵ More refined fits to the data could be obtained within the RAR model through a least squares analysis, when all halo observables are used to find the best fitting RAR free-parameters for $M_{\text{DM}}(r)$, besides the two (generic) halo restrictions here applied (to appear in Paper III dedicated to dSphs).

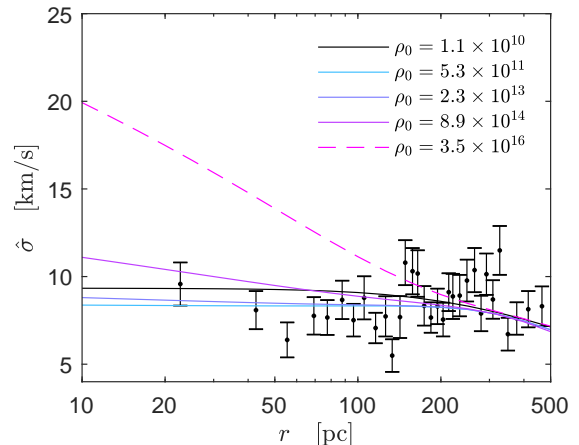


Figure 2: Comparison between the observed (projected) dispersion velocity ($\hat{\sigma}$) of Sculptor, taken from (Walker et al., 2009), against the same magnitude as predicted by a standard Jeans analysis. The latter uses the RAR benchmark solutions for the mass distribution $M_{\text{DM}}(r)$ as shown in fig. 1. Each solution is labeled with the central density in units of $M_{\odot} \text{pc}^{-3}$. Notice the fast rise in the inner-halo region (at \sim few 10 pc) due to the cuspy RAR halo with $\rho_0 = 3.5 \times 10^{16} M_{\odot} \text{pc}^{-3}$, implying a clear data mismatch in the case of this limiting dashed-magenta solution.

4.1.2. The UGC05986 spiral

In order to provide a complementary and detailed fit for a different galaxy type to the one shown in the above section, we have selected a DM dominated and well resolved spiral galaxy (UGC05986) from the Spitzer Photometry and Accurate Rotation Curves (SPARC) data base (Lelli et al., 2016). Specific information about each galaxy (i.e Hubble type, inclination etc) are provided in different files at <http://astroweb.cwru.edu/SPARC/>. We take for this galaxy the corresponding galactocentric radius r and rotation curves V , from the file Table2.mrt, as well as the baryonic contribution V_{bar} , composed of a bulge (V_{b}), disk (V_{d}) and gas component (V_{g}). The bulge and disk components are inferred from surface brightness observations for a given mass-to-light ratio. In sum, the baryonic component is given by

$$V_{\text{bar}}^2 = \Upsilon_{\text{b}} V_{\text{b}}^2 + \Upsilon_{\text{d}} V_{\text{d}}^2 + V_{\text{g}}^2 \quad (16)$$

With the corresponding mass-to-light *ratio factors* Υ_{b} and Υ_{d} for bulge and disk respectively. Then the rotation curve for each component traces immediately its centripetal acceleration $a = V^2/r$. We thus fit the inferred DM rotation curve, $V_{\text{DM}}^2 = V_{\text{obs}}^2 - V_{\text{bar}}^2$, with the Levenberg–Marquardt (LM) algorithm to find a χ^2 minima. The quantity χ^2 is calculated by

$$\chi^2(\mathbf{p}) = \sum_{i=1}^N \left[\frac{V_i - v(r_i, \mathbf{p})}{\sigma_i} \right]^2 \quad (17)$$

with N the number of data points, V_i is the set of circular velocity data, r_i is the corresponding set of radius data, $v(r_i, \mathbf{p})$ is the predicted circular velocity at radius

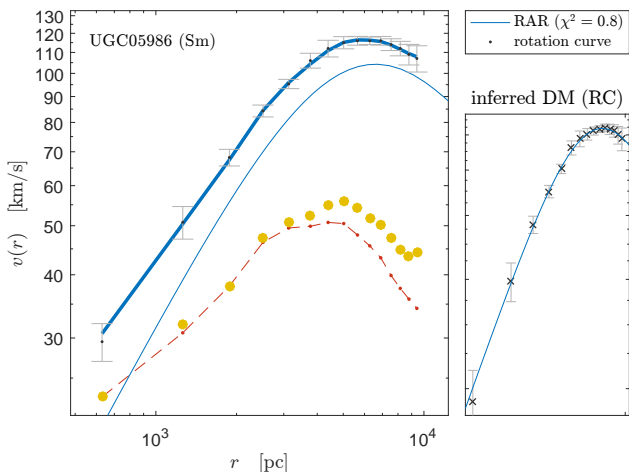


Figure 3: Best-fit of the RAR model for UGC05986, a dark matter dominated galaxy from the SPARC data base. Note also the well reproduced maxima of the total rotation curve (gray dots with error bars) as well as of the DM component (solid blue). The baryonic (stars + gas) component is shown as big yellow dots while stars only are shown as red dashed line.

r_i for the model parameter vector \mathbf{p} and σ_i is the uncertainty for V_i . For the RAR model under consideration, $\mathbf{p} = (\theta_0, W_0, \beta_0, m)$, we vary the three free parameter (θ_0, W_0, β_0) for a fixed particle mass $mc^2 = 50 \text{ keV}$ until the least square condition is satisfied, giving: $\beta_0 = 1.6 \times 10^{-7}$, $\theta_0 = 36.0$ and $W_0 = 64.5$.

In fig. 3 we show the rotation curves for different components of the galaxy UGC05986 as an example illustrating the necessity of cutoff effects for the DM dominated halo⁶. A detailed analysis of the full SPARC galaxy sample will be presented in an accompanying paper.

4.2. Particle mass dependence

In the case of typical dark halos in spiral, elliptical and BCGs a particle mass of $mc^2 = 48 \text{ keV}$ provides the maximum (critical) core mass of $M_c^{\text{cr}} = 2.2 \times 10^8 M_\odot$. If the mass is instead shifted to larger values, say $mc^2 \sim 100 \text{ keV}$, a different three-parametric (θ_0, β_0, W_0) family of solutions arises, able to reproduce the same DM halo observables (r_h, M_h) for each case. But now the maximum (critical) core mass decreases to $M_c^{\text{cr}} \sim 10^7 M_\odot$ for galactic structures larger than dwarfs. These new solutions have exactly the same core-halo behavior as those in fig. 1 with similar windows of *predicted* core and total halo mass (M_c and M_{tot}) but ending at the lower critical core mass as indicated above.

More generally, the fermion particle mass range $mc^2 \approx 48 - 345 \text{ keV}$, as obtained from the Milky Way analysis in Paper I, implies stable DM quantum cores with masses up

⁶Notice moreover from fig. A.8 (typical spirals) that $W_0 = 64.5$ lays within the range of benchmark solutions which correspond with the sharp decreasing halo tails (i.e. $\rho \propto r^{-n}$ with $n > 2$) in fig. 1

to the critical values. The lower particle mass the higher the critical core mass. Thus, the corresponding range is $M_c^{\text{cr}} \approx 4.2 \times 10^6 - 2.2 \times 10^8 M_\odot$ due to the particle mass dependence $M_c^{\text{cr}} \propto m^{-2}$ (see Argüelles and Ruffini, 2014).

4.3. About the critical core mass

The core of our configurations is supported by fermion degeneracy pressure. Therefore, the core is subjected to the gravitational instability leading to the concept of critical mass, traditionally introduced for white dwarfs (Anderson, 1929; Stoner, 1930; Chandrasekhar, 1931a,b; Landau, 1932) and neutron stars (Oppenheimer and Volkoff, 1939; Rhoades and Ruffini, 1974). When the pressure is dominated by the degeneracy pressure (i.e. when the temperature is much lower than the Fermi temperature), the fermion kinetic energy depends only on density, and so the equilibrium value of mass and radius of the configuration is set by the balance between the gravitational and the kinetic energy, at given finite density (Oppenheimer and Volkoff, 1939). This effect can already be seen in a post-Newtonian approximation determination of the equilibrium configurations (see e.g. Wagoner and Malone, 1974; Ciufolini and Ruffini, 1981). It can be shown that such a limiting configuration is the first turning-point of the equilibrium sequence of increasing central density, namely configurations along the sequence branch with $dM/d\rho_c > 0$ are stable, the ones with $dM/d\rho_c < 0$ are unstable, and $dM/d\rho_c = 0$ is the turning point, the critical mass configuration (see Shapiro and Teukolsky, 1983, for a detailed discussion on the subject). The above concept of the critical core mass M_c^{cr} can be therefore formally achieved by finding the maximum (turning point) in a ρ_0 vs. M_c diagram, as was shown in the context of the original RAR model, i.e. for $W_0 \rightarrow \infty$ (see Argüelles and Ruffini, 2014, and references therein). Labeled here as the *critical-core* condition, this concept applies in the same way for the actual RAR model with cutoff ($W_0 < \infty$), see fig. 4.

Accordingly, typical spiral and elliptical galaxies as well as BCGs reach the critical core mass (e.g the turning point at a critical density), corresponding to a critical temperature parameter β_0^{cr} . For typical dwarfs, on the other hand, the maximal temperature ($\beta_0^{\text{max}} < \beta_0^{\text{cr}}$) is set by the astrophysical condition, such as requiring a maximum in the rotation curve on halo scales. The (i.e. for $\beta_0 > \beta_0^{\text{max}}$ such condition is broken as explicit in the dashed solutions of fig. 1 for dwarfs). This limits the maximal core mass (and central density), being far away from the critical value.

4.4. Role of the degeneracy and cutoff parameters in the core-halo morphology of RAR solutions

The fact that higher compactness of the core is obtained by increasing the temperature parameter, while maintaining a rather low degeneracy, is understood by the semi-degenerate nature of our fermionic solutions in contrast with a fully degenerate regime. The combination of

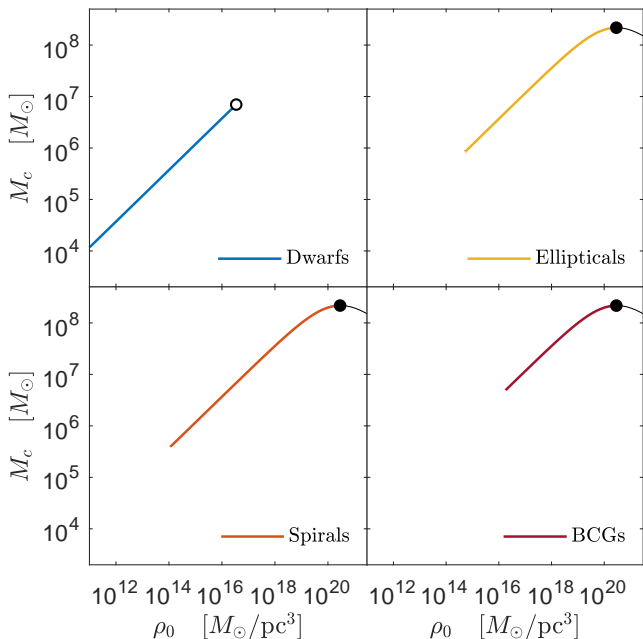


Figure 4: Explicit calculation of the $\rho_0 - M_c$ parameter space within the RAR model for $mc^2 = 48 \text{ keV}$ in the case of typical dwarf (blue line), spiral (red line), elliptical galaxies (yellow line) and BCGs (tamarillo line). Each type is described by given halo observable conditions (M_c and r_h). Notice the case of spirals, ellipticals and BCGs where a critical DM core mass $M_c^{\text{cr}} = 2.2 \times 10^8 M_\odot$ is reached at the maximum of the curve, when studied through the turning point criterion for core collapse in the $\rho_0 - M_c$ plane (see e.g. Argüelles and Ruffini, 2014).

the finite-temperature effects and the monotonically decreasing change (from positive to negative values) of the degeneracy parameter with the distance (see e.g. upper panel of fig. 2 in Argüelles et al., 2018) are the responsible for the clear *dense quantum core - Boltzmannian tail* behavior of the density profiles in fig. 1. Once in the diluted regime, and for solutions which are still away from becoming critical, a small increase in W_0 has important effects on the RAR halo scales: the larger the cutoff parameter W_0 , the more massive and more extended the galaxy gets as can be directly checked in fig. 1 and fig. A.8 from dSphs to ellipticals to BCGs, respectively.

This fact is better understood through the role of the escape energy $\varepsilon(r)$ in the distribution function (see sec:RAR-model). The larger the escape energy $\varepsilon(r) \neq \infty$, the larger the momentum (and energy) space the particles can occupy at any radius. Note, the escape energy is proportional to the cutoff parameter $W(r)$. In consequence, the solution cover more extended total spatial extensions before $W(r)$ reaches 0 at the boundary radius r_b .

5. Galaxy parameter correlations

In the previous sections we have successfully compared and contrasted the solutions of the RAR model with a wide range of galactic observables. We turn now to analyze if

the RAR model agrees with the following observational correlations:

- The constancy of the *central* surface DM density in galaxies, e.g. $\rho_{0D} r_0 \approx 140_{-50}^{+80} M_\odot \text{pc}^{-2}$. It spans about 14 orders of (absolute) magnitude (M_B), where ρ_{0D} and r_0 are the *central* DM halo density at the one-halo-scale-length of the Burkert profile (Donato et al., 2009).
- The $M_{\text{BH}} - M_{\text{tot}}$ relations with M_{BH} the mass of the compact dark object at the centre of galaxies and M_{tot} the total DM halo mass (Ferrarese, 2002; Kormendy and Bender, 2011; Bogdán and Goulding, 2015).

In order to show this, we use the full family of astrophysical RAR solutions (i.e. contained within the blue-shaded region of fig. 1) for typical dSphs, spiral and elliptical galaxies as well as typical BCGs. Such solutions cover the maximal free parameter space (β_0, θ_0, W_0) for each galaxy type as constrained by the halo observables (r_h, M_h) for the particle mass $mc^2 = 48 \text{ keV}$ together with the *quantum core* condition. Correspondingly, a well defined window of predicted masses (M_c, M_{tot}) is obtained (see fig. A.7 for details). As we show below, the knowledge of the corresponding values of the plateau density ρ_{pl} is also important for the analysis of the *central* surface DM density relation.

We can proceed now to make a consistency check of the predictions of the RAR model by contrasting them within the physical observed spread of the correlations. Notice that the constancy of the *central* surface DM density deals only with DM halos while the $M_{\text{BH}} - M_{\text{tot}}$ relations correlate both, the central and total halo dark object masses. Traditionally, the central compact dark objects are assumed as supermassive Black Holes (SMBHs). But here we interpreted them as DM quantum cores with the exception of active galaxies harboring supermassive central objects above $\sim 2 \times 10^8 M_\odot$.

5.1. DM surface density relation

Regarding the *central* surface DM relation, we first take from the literature the values for the blue absolute magnitude M_B , corresponding to each typical galaxy within each galaxy type considered above. Thus we adopt $M_B \approx -10.2$ for typical dSphs (Irwin and Hatzidimitriou, 1995), $M_B \approx -20.8$ for the Milky Way (Karachentsev et al., 2004), $M_B \approx -20.5$ for typical spirals (de Blok et al., 2008), $M_B \approx -21.5$ for typical ellipticals (Hoekstra et al., 2005) and $M_B \approx -23$ for typical BCGs (Wing and Blanton, 2013).

Then, in order to calculate the DM surface density $\Sigma_{0D} = \rho_{0D} r_0$ in each case, we simply realize that the equivalent of the Burkert central density ρ_{0D} would correspond to the density of the plateau ρ_{pl} within the RAR model. The relation between both one-halo scale lengths is given by

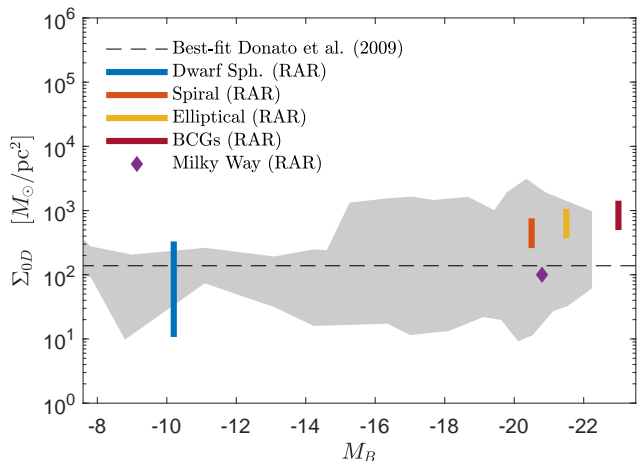


Figure 5: The surface DM density as predicted by the RAR model (see vertical colour lines) for each galactic structure in correspondence with the astrophysical solutions (i.e. blue-shaded regions in fig. 1). The dashed horizontal line represents the Universal relation from the best fit of the data as found by Donato et al. (2009). The dark-gray region indicates the delimited area by the $3 - \sigma$ error bars of all the data points. The result shows the ability of the three parametric RAR model (for $mc^2 = 48$ keV) to be in agreement with the DM surface density observations (see text for further details regarding BCGs).

$r_0 \approx 2/3r_h$, where r_h is fixed for each galaxy type according to the imposed halo constraints. For the corresponding family of ρ_{pl} values see table 1 and fig. A.7.

We thus calculate the product $2/3\rho_{\text{pl}}r_h$ for each theoretical profile in the case $mc^2 = 48$ keV, including the Milky Way, and finally contrast the pair (M_B, Σ_{0D}) with the observational relation found by Donato et al. (2009).

The results for dwarfs to ellipticals are in very good agreement with the observed relation, see fig. 5. For simplicity, the latter is displayed as the overall dark-grey region delimited (or enveloped) within the $3 - \sigma$ error bars along all the data points considered in Donato et al. (2009). The predicted surface density (vertical solid lines), for the adopted M_B values, are located within the expected $3 - \sigma$ data region. The magnitude M_B of typical BCGs is beyond the observed window reported in Donato et al. (2009) who considered up to elliptical structures, but their predicted values are somewhat similar to the latter.

Remarkably, our results of the RAR model show a mild increasing behavior with decreasing M_B . This trend resembles the analogous universal relation presented in Boyarsky et al. (2009) where larger elliptical galaxies as well as clusters were included in the analysis, contrary to the sample presented in Donato et al. (2009).

5.2. Super massive central object - DM halo mass relation

Concerning the $M_{\text{BH}} - M_{\text{tot}}$ relations, we show in left-panel of fig. 6 the predicted (M_c, M_{tot}) values (see also fig. A.7) for many different astrophysical family of RAR solutions including (but not limited to) the typical galactic

structures of fig. 1), together with the observationally inferred best-fit relations found in Ferrarese (2002); Bogdán and Goulding (2015). The observational inferred relations are limited to the region where data supports, i.e. the *Ferrarese strip* denoted by blue-ish area in left-panel of fig. 6. Interestingly such observational strip is explicitly shown to be contained (up to $M_c \sim 10^8 M_\odot$) within the larger RAR green-ish predicted area from small spirals up to ellipticals. The red and yellow continuous thick L-shaped lines correspond to the typical spirals and ellipticals considered in section 3. While the thin white lines (labeled with different M_{tot} values) cover many different one-halo scale observables (r_h, M_h) besides the ones associated to the typical galactic structures introduced in section 3. Such new (r_h, M_h) values are obtained from the *independent* Donato relation as explained in Appendix C and fig. C.10, with the aim to maximally cover the (M_c, M_{tot}) plane. The RAR predicted (green-ish) area extends out of the Ferrarese strip, indicating a potential window of core-halo masses which are either not yet observed or unphysical.

Indeed, RAR solutions deviating too far-left of the observed strip (e.g. dot B in left-panel of fig. 6), has isothermal-like density tails ($\rho(r) \sim r^{-2}$) as plotted in right-panel, at difference with RAR solutions lying along the best-fit relation (e.g. dot b, see both panels). The later has halo tails decreasing as $\rho(r) \propto r^{-3}$ somewhat inside r_h ⁷ more in line with other phenomenological profiles arising from N-body simulations either in WDM or CDM cosmologies. From this comparison we can conclude that the observed (M_c, M_{tot}) correlation *disfavors* RAR solutions showing isothermal-like halo tails, while favors more sharply decreasing halo tails. The Milky Way RAR solution is also plotted for completeness, showing a good agreement as well.

The case of typical dwarf galaxies (thick blue curve) is located at the lower-left end of the (M_c, M_{tot}) plane in fig. 6, beyond the observationally inferred blue-ish strip. It is worth to stress that no observational data exist yet in that part of the correlation and thus the obtained results are considered as a pure RAR model prediction, subject to observational scrutiny. However, special attention has to be given to our dwarf galaxy predictions in view of the recent observational reports of putative massive black holes of few $\sim 10^6 M_\odot$ detected in ultra-compact dwarf galaxies of total mass of few $\sim 10^7 M_\odot$ (e.g. Seth et al., 2014; Ahn et al., 2017, 2018; Afanasiev et al., 2018). Similarly interesting candidates are the recent discovered intermediate-mass Black Holes (IMBHs) in globular clusters (e.g. Kızıltan et al., 2017; Perera et al., 2017).

When we look at larger structures beyond ellipticals we find BCGs as further convenient predictions. Interestingly (and different to the other smaller structures considered) their dark central cores are limited by a relatively light-

⁷ Due to the cut-off effects, the RAR halo tails behaviour for solutions which are favored by the correlation are of polytropic nature, with $\rho \sim r^{-4}$ for $r = r_h$.

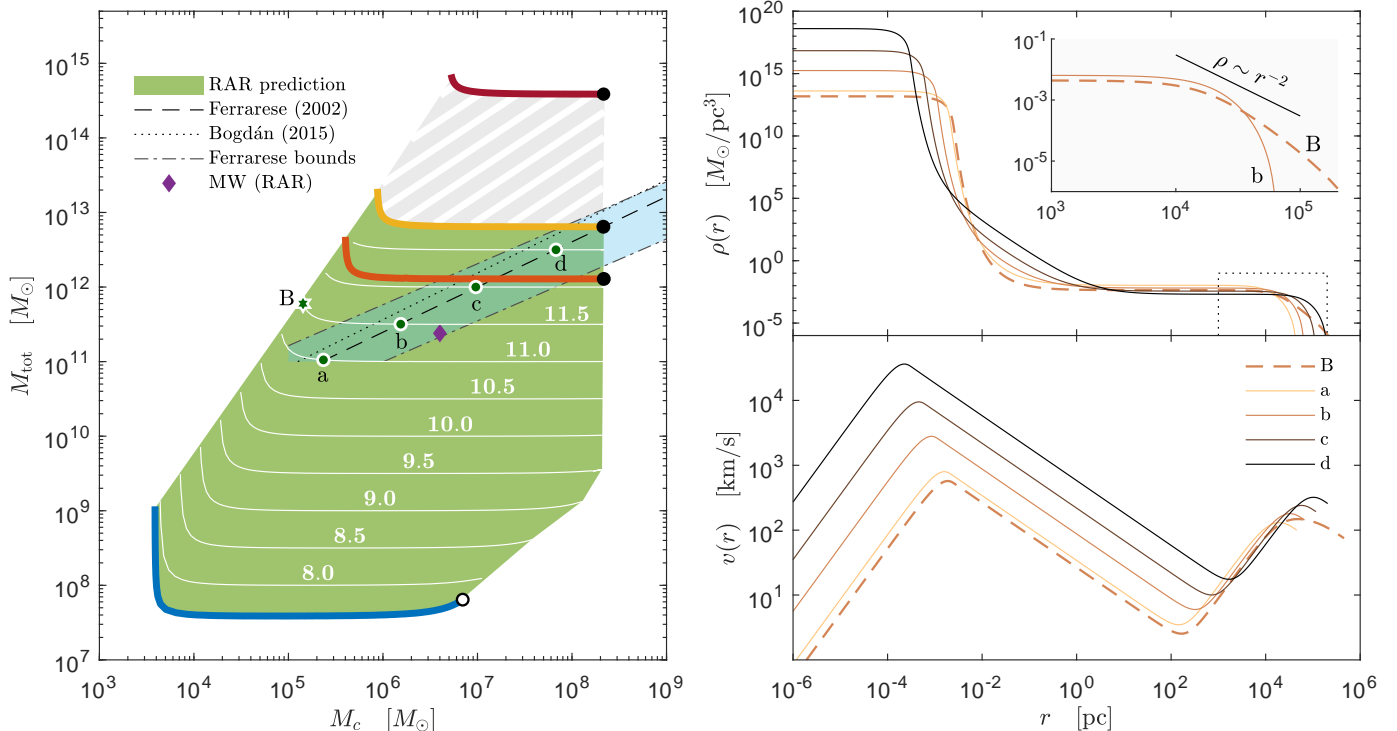


Figure 6: **(left)** Prediction of the $M_c - M_{\text{tot}}$ relations within three parametric RAR model (for $mc^2 = 48 \text{ keV}$). The different coloured lines read for each galaxy type in correspondence with the astrophysical RAR solutions as given in fig. 1. The green area, on the other hand, covers all RAR predictions for a given halo mass in the range $M_h \approx 10^7 - 10^{12} M_\odot$ and fulfilling $\frac{2}{3}\rho_{\text{pl}}r_h = 140 M_\odot/\text{pc}^2$ as inferred from the Donato relation. The white lines show a set of families with given halo mass M_h (and labeled by the M_{tot} value in the horizontal regime). The results show the ability of the RAR model to be in agreement with the different $M_{\text{BH}} - M_{\text{tot}}$ relations, as considered in the literature, and explicated in the blue-ish stripe. The shaded area above ellipticals is just the extrapolation of the $M_c - M_{\text{tot}}$ RAR prediction for BCGs obtained assuming the constant (best fit) of the Donato relation (see also Appendix C). The filled-black dots correspond to the critical core mass M_c^{cr} , and the empty-black dot indicates the limiting maximum core mass M_c^{max} for dwarfs. **(right)** Density and velocity profiles associated with the 4 benchmark solutions of the left panel labeled by (a-d). Such solutions lie along the best-fit of Ferrarese (2002) with the given mean surface density $\frac{2}{3}\rho_{\text{pl}}r_h = 140 M_\odot/\text{pc}^2$. While the dashed curve (B) representing an isothermal-like RAR solution (corresponding with dot B in left-panel) is clearly disfavored by the observed correlation, the continuous curves (as e.g. (b)) are favored.

mass value ($M_c^{\text{cr}} \sim 2 \times 10^8 M_\odot$) when compared to the very massive halo of few $10^{14} M_\odot$. Having halo properties very similar to typical ellipticals and spirals, in line with the universal DM halo morphology within the standard picture of hierarchical structure formation.

Notice that a vertical trend up to infinity (not shown) in the L-shaped lines of fig. 6 corresponds to RAR solutions having the minimum core mass (or minimum ρ_0) which in turn implies the larger cutoff parameters until $W_0 \rightarrow \infty$ with no particle escape whatsoever (see fig. A.7 for the case of typical galactic structures). Those solutions develop more extended and more massive halos. Such trend ends in an infinite halo mass when the limiting $\rho \propto r^{-2}$ isothermal RAR tail is reached, unless some (extra) virial condition is imposed to them (e.g. typically setting a minimum threshold density at about $\sim 200\rho_{\text{cr}}$ to any profile, where ρ_{cr} is the critical density of the Universe). Solutions with total masses exceeding such virial constraint are excluded as astrophysical ones and therefore not appearing in fig. 6.

It is appropriate to stress at this point that the M_{tot} values appearing in the observed relations plotted in fig. 6,

were calculated at the virial radius within a Navarro-Frenk-White DM model (Ferrarese, 2002). While in our case, they were obtained at the surface radius r_b of the RAR model equilibrium configurations. Besides, the majority of the values of M_{BH} in the observed $M_{\text{BH}} - M_{\text{tot}}$ relation have been obtained through the so-called $M_{\text{BH}} - \sigma_*$ relation, with σ_* the bulge dispersion velocity (Ferrarese and Merritt, 2000; Gebhardt et al., 2000; Gültekin et al., 2009). However, in the case of dwarf galaxies the observational inference of the dark central object mass via the dispersion velocity is unclear (see, e.g., Valluri et al., 2005; Kormendy and Bender, 2011, and references therein). Interestingly, Valluri et al. (2005) attempted to give an estimate of such a central object mass in the case of NGC205 obtaining $M_{\text{BH}} \sim 10^3 - 10^4 M_\odot$ (interpreted there as an IMBH), which is in agreement with the values of M_c for the typical dSphs analyzed in this work (see table 1).

Finally, in the case of larger elliptical galaxies, it is interesting to note that the maximum quantum core mass $M_c^{\text{cr}} \sim 2 \times 10^8 M_\odot$ (for $mc^2 = 48 \text{ keV}$) predicted by our model, is in striking consistency with the uppermost (sample-

representative) central mass M_{BH} obtained in [Bogdán and Goulding \(2015\)](#), from an X-ray imaging analysis of more than 3000 isolated and without AGN activity elliptical galaxies. These results, when viewed through our theoretical $M_{\text{BH}} - M_{\text{tot}}$ relation, give support to our idea that normal elliptical galaxies may harbor dark central objects (not yet BHs) without showing AGN-like activity, while larger SMBHs masses, do show AGN properties, reaching the upper end of the $M_{\text{BH}} - M_{\text{tot}}$ relation.

Additional verification of the above predictions of the RAR model needs the observational filling of the gaps in the (M_c, M_{tot}) plane from dwarfs all the way up to ellipticals. This has been partially done for disk galaxies from the SPARC data base and will be presented in an accompanying paper.

6. Concluding remarks

In Paper I we clearly demonstrated that gravitationally bounded systems based on fermionic phase-space distributions including for escape velocity effects and central degeneracy, can explain the DM content in the Galaxy while providing a natural alternative for the central BH scenario in SgrA*. This highly compelling result is bolstered here by the analysis of different galactic structures ranging from dwarfs to ellipticals to galaxy clusters.

As an interesting example, we have discussed in this paper the solutions for $mc^2 = 48 \text{ keV}$, where the model is able to explain the DM halos from typical dSph to normal elliptical galaxies up to typical BCGs, and predict the presence of massive compact dark objects from $\sim 10^3 M_\odot$ up to $\sim 10^8 M_\odot$ at their respective centers. A key point of the present RAR model is the ability to fulfill the observed properties of galaxies, such as the $M_{\text{BH}} - M_{\text{tot}}$ and the $\Sigma_{\text{OD}} \approx \text{const}$ universal relations, for a unique DM fermionic mass. The versatility of the physical three-parametric solutions, can also account for the (real) physical spread observed in the correlation between dark halo mass Vs. dark central object mass, as observationally inferred in [Ferrarese \(2002\)](#); [Kormendy and Bender \(2011\)](#); [Bogdán and Goulding \(2015\)](#). Whether or not such full window of compact dark-object masses at the centres of galaxies occur in Nature is a theme of future observational works, particularly interesting in the case of the smallest (i.e. faintest) dwarf galaxies.

Nevertheless, the analysis should cover all observed plethora of galactic dark halos with corresponding dark compact central objects. In particular, the RAR model predicts that galaxies with similar halo properties (i.e. total halo mass and radius) can harbor different dark quantum core masses, spanning up to about 3 orders of magnitude. This peculiar feature is an important result of our theory, considering that very similar Seyfert-like galaxies have been observed to shown values of M_c that can differ in nearly one order in magnitude ($M_c \sim 1 \times 10^7 - 8 \times 10^7 M_\odot$, see [Greene et al., 2010](#)).

At the upper limit of the compact core mass range, it provides, on astrophysical basis, possible clues on the formation of SMBHs in galactic nuclei. In the case of typical dark halos in normal spiral and elliptical galaxies, self-gravitating fermions with a particle mass of 48 keV may produce a maximum (critical) core mass of $M_c^{\text{cr}} = 2.2 \times 10^8 M_\odot$, at the onset of gravitational collapse.

The majority of the supermassive dark central objects are comprised within $M_c \sim 10^8 M_\odot$ ([Gültekin et al., 2009](#)). However, in the largest elliptical galaxies have been also observed more massive dark objects up to $\sim 10^{10} M_\odot$. Those candidates are most likely SMBHs associated with active galaxies and are characterized by a clear X-ray and radio emissions as well as jets. Such SMBHs may be explained starting from a BH seed of mass M_c^{cr} formed out of the collapse of our critical quantum DM cores. After its formation, such a BH seed might start a baryonic and/or dark matter accretion process from their massive galactic environment ($M_g \sim 10^{12} M_\odot$). An accretion of $\sim 1\%$ of the (inner) baryonic mass of the galaxy onto the M_c^{cr} core mass obtained here, would be enough to explain the formation of the largest ($M_{\text{BH}} \sim 10^9 - 10^{10} M_\odot$) SMBH masses.

Other observational data-sets such as Ly α forest constraints, or high resolution rotation curves of disk galaxies (points (b) and (c) mentioned in the introduction), are also important to discriminate between different particle-motivated DM halo models such as the RAR model, FDM or sub-keV degenerate fermions. Standard FDM as the ones recently considered in [Hui et al. \(2017\)](#), has an associated matter power spectrum which share the same features with the one of the WDM paradigm at large scales, both exhibiting a clear drop (though somewhat different in shape) in power below a given scale ([Marsh and Silk, 2014](#)). Such similar behaviour allowed [Hui et al. \(2017\)](#) to roughly relate the lower bound mass values of FDM to the ones of a WDM fermion obtained by [Viel et al. \(2013\)](#) from Ly α forest data. In particular, a lower limit of $2.5 \text{ keV}/c^2$ (at $3 - \sigma$) of the hypothetical WDM particle (thermal relics) translates into $m_b c^2 > 10^{-21} \text{ eV}$ for the ultra light boson at the same confidence level ([Hui et al., 2017](#)). Unfortunately, this bound strongly disfavours the typical FDM range of masses needed to solve different small-scale issues of the CDM paradigm ([Hui et al., 2017](#)). Improved analysis making use of dedicated cosmological simulations within FDM paradigm to account for the physics at the scales probed by the Ly α forest data (from the BOSS survey), exclude the mass range $m_b = 10^{-22} - 2.3 \times 10^{-21} \text{ eV}$ ([Armengaud et al., 2017](#)).

In the case of fermionic models, it is then clear from the above paragraph that the $\sim \text{few keV}$ lower bound found in [Viel et al. \(2013\)](#), see also [Yèche et al. \(2017\)](#) for more general lower bounds above keV including for sterile neutrino WDM) is in tension with the below-keV Thomas-Fermi DM models presented in [Destri et al. \(2013\)](#); [Domcke and Urbano \(2015\)](#); [Randall et al. \(2017\)](#), while it remains in agreement with the RAR model here presented.

Reproducing the (total) Milky Way rotation curve features poses as well serious challenges to FDM models in the desired mass range needed to account for other astrophysical and small-scale cosmological observables (Bar et al., 2018). Indeed, it was there explicitly shown that the solitonic core arising typically at bulge-scales in the case of typical disk galaxies, practically excludes the FDM mass range $m_b = 10^{-22} - 10^{-21}$ eV. Finally, the case for highly degenerate fermionic halos (i.e. Thomas-Fermi models DM cited above), are not applicable at all to reproduce the rotation curves of disk galaxies (or larger), since they were originally motivated to fit the dispersion velocities of small dSphs (Destri et al., 2013) due to the predicted highly compact and small sized halos. Moreover, a closer look on such models (as the one recently analyzed in Domcke and Urbano (2015)) shows that they are disfavoured even to fit dSph dispersion velocities, and the artificial introduction of an isothermal tail is needed (Randall et al., 2017).

Thus, the results described in the above paragraphs put the RAR model with fermion masses above 10 keV, in a position of privilege with respect to other particle-based models such as FDM or the ones based on sub-keV fully-degenerate fermions.

Finally, and in order to attempt to answer the question why nature constrains the RAR model free parameters to the specific values shown in fig. A.8 and table 1, it would need the extension of the present analysis into a broader theoretical context such as the formation and evolution of galaxies.

Such an insight may be likely gained through a detailed study of a dynamical theory of collisionless relaxation, including a full statistical/thermodynamical analysis of the condition under which (quasi) DM halo relaxation is reached. Considerations based on maximization entropy approaches for given total mass (with corresponding running of the free model parameters), as the one analyzed in similar self-gravitating systems in Chavanis et al. (2015) (and references therein), could help in this direction. These interesting aspects are out of the scope of the present work and are subject of future research.

Acknowledgments

We thank the referee for her/his very constructive and clear suggestions. C.R.A acknowledges support by the International centre for Relativistic Astrophysics Network (ICRANet) and CONICET-Argentina. J.A.R acknowledges support from the International Cooperation Program CAPES-ICRANet financed by CAPES-Brazilian Federal Agency for Support and Evaluation of Graduate Education within the Ministry of Education of Brazil. A.K. is supported by the Erasmus Mundus Joint Doctorate Program by Grants Number 2014-0707 from the agency EACEA of the European Commission.

Appendix A. Parameter space analysis

Here we show how the halo observable constraints (r_h and M_h) together with the additional *quantum-core* condition define the limiting values of the free sets of RAR configuration parameters (β_0, θ_0, W_0) for the different galaxy types. Specifically fig. A.8 shows the full curves in the (β_0, θ_0, W_0) -space for $mc^2 = 48$ keV. Each galaxy is represented through a coloured 1-dimensional line, i.e. in thick blue (dwarfs), red (spirals) and yellow (ellipticals), while typical BCGs are represented through a thick tamarillo line. We also include along each line the sets of the 5 benchmark RAR solutions, given in fig. 1, through dots in corresponding colours. This correspondence shows clearly the ranges of β_0 , θ_0 , and W_0 , encompassing all the astrophysical RAR solutions.

Appendix A.1. About the 1-dimensional curves of free RAR model parameter space

The fact that the halo scale radius r_h sets a specific morphological point in the RAR solutions (i.e. as in $v_{\text{DM}}(r)$, $M_{\text{DM}}(r)$, $\beta(r)$, $\theta(r)$, etc.), it must necessarily depend on the specific choice of the initial conditions, i.e.

$$r_h \equiv r_h(\beta_0, \theta_0, W_0, m)$$

This functional dependence, together with

$$M_h \equiv M_{\text{DM}}(\beta_0, \theta_0, W_0, m, r_h)$$

clearly defines a 1-dimensional curve in the (β_0, θ_0, W_0) RAR configuration parameter space once m , M_h and r_h are given (i.e. 4 free parameters and 3 constraints).

The number of free parameters of the model may be reduced to three when the particle mass m is set (i.e. in the range $mc^2 \approx 48 - 345$ keV as obtained in PaperI). This approach requires only 2 constraints, such as r_h and M_h . If instead only one constraint (i.e. $M(r)$ with $r \neq r_h$ a hypothetically well constrained halo scale-length) is applied instead of the two constraints used in this work, then a narrow 2-dimensional region would arise in the (β_0, θ_0, W_0) -space of fig. A.8. Nevertheless, many of the solutions in this (more) extended family will certainly provide worst fits to the baryonic data (as e.g. for the case of $\hat{\sigma}$ in dSphs) than the solutions here presented, considering less observable constraints were used.

Appendix A.2. Limiting behavior in the parameter sets

The effects of the RAR parameter sets in the corresponding RAR solutions explain the limiting values in the core mass M_c , the total mass M_{tot} and plateau density ρ_{pl} . The maximum and minimum DM masses, predicted by the RAR model, have associated maximum and minimum in the predicted ρ_{pl} values, as explicitly shown in fig. A.7.

The importance of those predicted windows for each galaxy type reflects universal relations between galaxy parameters. Thus, the predicted windows of M_c and M_{tot}

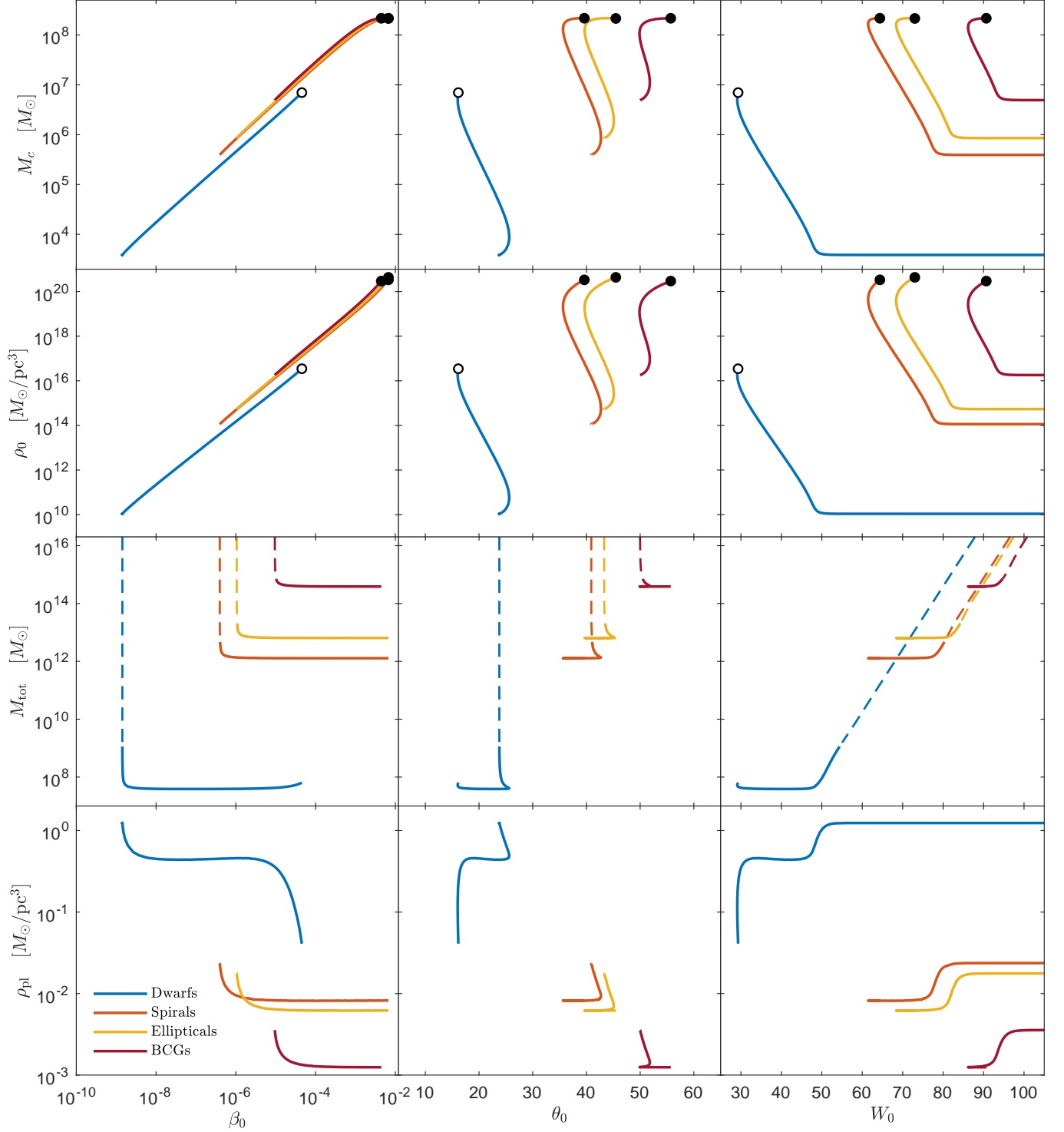


Figure A.7: Full display of RAR magnitudes ($\rho_0, M_c, M_{\text{tot}}$, and ρ_{pl}) for $mc^2 = 48 \text{ keV}$ as a function of β_0 (left column), θ_0 (central column) and W_0 (right column). The dashed-lines in the M_{tot} row correspond with isothermal-like halo tails having densities *below* the virial value $\sim 200\rho_{\text{cr}}$ as set in section 5. Shown are three typical galaxy types (dwarfs, spirals, ellipticals) and typical BCGs representing larger structures. Each case is constrained by halo observables (r_h and M_h). The existence of a critical core mass of $M_c^{\text{cr}} = 2.2 \times 10^8 M_\odot$, for the case of typical spiral and elliptical galaxies as well as BCGs, is denoted by a filled black dot. In the case of dwarfs there is only a maximum value β_0^{max} (with associated M_c^{max}) and denoted by an empty black dot. Notice also the larger RAR plateau density ($\sim 10^{-1} M_\odot/\text{pc}^3$) for the dwarf galaxies (on inner-halo scales) with respect to the corresponding lower values for larger galactic structures (in line with observations, see e.g. Walker et al. (2009)).

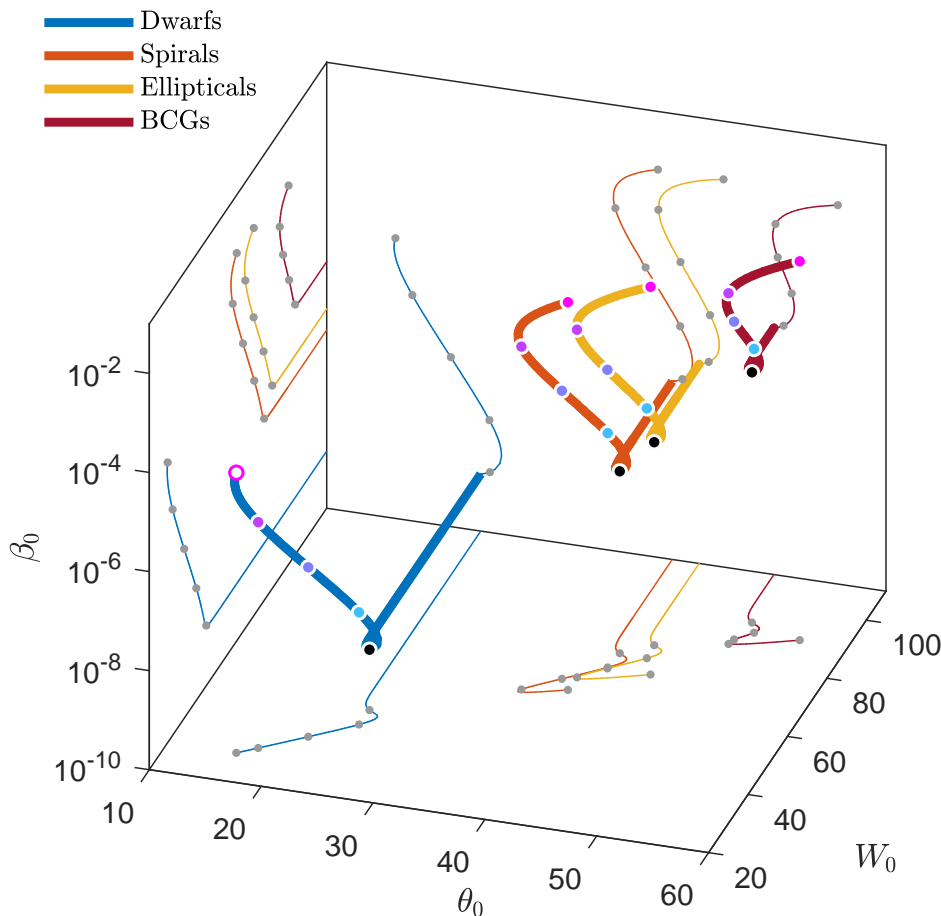


Figure A.8: Full astrophysical ranges of the configuration parameters for $mc^2 = 48 \text{ keV}$. Specific observational halo constraints (M_h and r_h) for each astrophysical case define 1-dimensional curves in the (β_0, θ_0, W_0) -space. Each coloured dot along each thick line has its corresponding RAR benchmark solution (for $M_{\text{DM}}(r)$, $v_{\text{DM}}(r)$ and $\rho(r)$) in fig. 1. The limiting filled-magenta dots correspond to the critical solutions for spirals, ellipticals and BCGs while the empty-magenta dot is associated with the limiting (non-critical) solution for typical dwarfs. The latter is set by the (threshold) solution without developing a maximum in the halo rotation curve. The straight line behaviour in all cases correspond to solutions having the minimum core mass (or minimum ρ_0), as well as achieving the more extended density tails as can be seen from fig. 1. These solutions develop isothermal-like tails, ending in the standard isothermal density tail $\rho \propto r^{-2}$ for infinitely large cut-off parameter W_0 .

masses reflect the Ferrarese Universal relation (Ferrarese, 2002) while the predicted ρ_{pl} window reflects the constancy of the *central* surface DM density in galaxies (Donato et al., 2009). Both relations are discussed in detail in section 5.

The main responsible for the increase of the quantum-core mass, i.e. from $\sim 10^3 M_\odot$ in dSphs to $\sim 10^8 M_\odot$ in typical spirals, ellipticals and BCGs, is the temperature parameter β_0 , which can vary about six orders of magnitude among the different galaxy types. Instead, the pair (θ_0, W_0) remains around the same order-of-magnitude values and is mainly relevant to the DM halo physics. For the latter compare fig. 1 and fig. A.8, together with values in table 1.

The temperature parameter β_0 is limited from above by its critical value β_0^{cr} for the case of typical spiral and elliptical galaxies as well as BCGs. That limit is set by the *quantum core* condition. For higher values the RAR solutions become gravitationally unstable and lead to the

gravitational collapse of the quantum core. In the case of typical dwarf galaxies the temperature is limited by its maximum value β_0^{max} . That limit, on the other hand, is set by the (threshold) solution without a maximum in the halo rotation curve, corresponding to highly cuspy halos. Thus, while β_0^{cr} sets the critical core mass M_c^{cr} for typical spiral and elliptical galaxies as well as BCGs, the β_0^{max} sets the M_c^{max} for typical dSphs. See fig. A.7 and table 1 for numerical values for each galaxy type.

At the same time, a specific minimal temperature parameter β_0^{min} (for all galaxy types and BCGs) is implied by the linear relation between the configuration parameters (β_0, θ_0, W_0) , as seen in fig. A.8 and the corresponding projection-planes (for β_0 not close to its maximum). For large enough W_0 values (and beyond) the solutions develop isothermal halo tails without affecting the inner structures through surface effects. Especially, the core remains constant, what resembles here mainly constant β_0 and θ_0

values. Thus, large enough W_0 values set all the possible total halo masses M_{tot} , although unbounded from above because W_0 may grow up to infinity. Correspondingly those solutions imply the minimal temperature β_0^{min} which produce minimal DM core masses (see the W_0, β_0 projection plane).

The existence of a β_0^{cr} for spirals, ellipticals and BCGs (and β_0^{max} for dwarfs), will necessarily define through the above monotonic relation a low enough W_0 value to set the minimal total halo mass for each galaxy type. In the case of spirals, ellipticals and BCGs that minimum correlates with the maximal (critical) temperature β_0^{cr} . The correlation does not apply for dwarfs due to the strong boundary effects (i.e. small-sized) close to the maximal temperature β_0^{max} , see fig. A.7.

Appendix B. Robustness of the RAR model predictions

The allowed choice for observational constraints at the rotation curves maxima (r_h, M_h), are here selected in order to have a convenient and unique prior to be used across the entire galaxy zoo. Nevertheless, more precise observational halo mass constraints can be obtained at other typical radial halo scales (though somewhat close to r_h), depending on the galaxy type. For example, in the case of dSphs, the halo mass is observationally better constrained at r_{300} (i.e. at 300 pc, very close to r_{half} for Milky Way satellites) as shown in Strigari et al. (2008). Including spiral and elliptical galaxies, other typical one-halo scale lengths (such as the Burkert halo scale-length) are appropriate as reported in Donato et al. (2009).

With the aim to analyze the robustness of the RAR model predictions, we further investigate which are the effects on the free RAR model parameters when changing the halo constraints (r_h, M_h) to the (observationally) better constrained couple ($M(r_{300}), M(r_{\text{last}})$). Here, r_{last} is the last observed data point, as reported in Walker et al. (2009), allowing for a good fit of $M(r_{\text{last}})$. These constraints represent the case of typical dSphs.

The results show a mild shift between the new set of astrophysical RAR solutions, illustrated as a light-red shaded region in fig. B.9, with respect to the one already found in fig. 1 (displayed as grey-shaded region in fig. B.9). Correspondingly, we found similar sets of free RAR free model parameters for the new benchmark solutions, as explicated in table B.2, which should be compared with those in table 1.

It is worth to note that with the new set of constraints our results predict a narrower range for the core mass, $M_c \approx 4.3 \times 10^3 - 3.8 \times 10^6 M_\odot$, compared to the result in section 4. This is an increase of about 10% for the lower limit and a decrease of about 46% for the upper limit. The total mass shows an offset towards higher values with increase of about 200 – 250%.

Similarly, the same results predict also a narrower range for the surface density $2/3\rho_{\text{pl}}r_h \approx 19.5 - 78 M_\odot/\text{pc}^2$, being

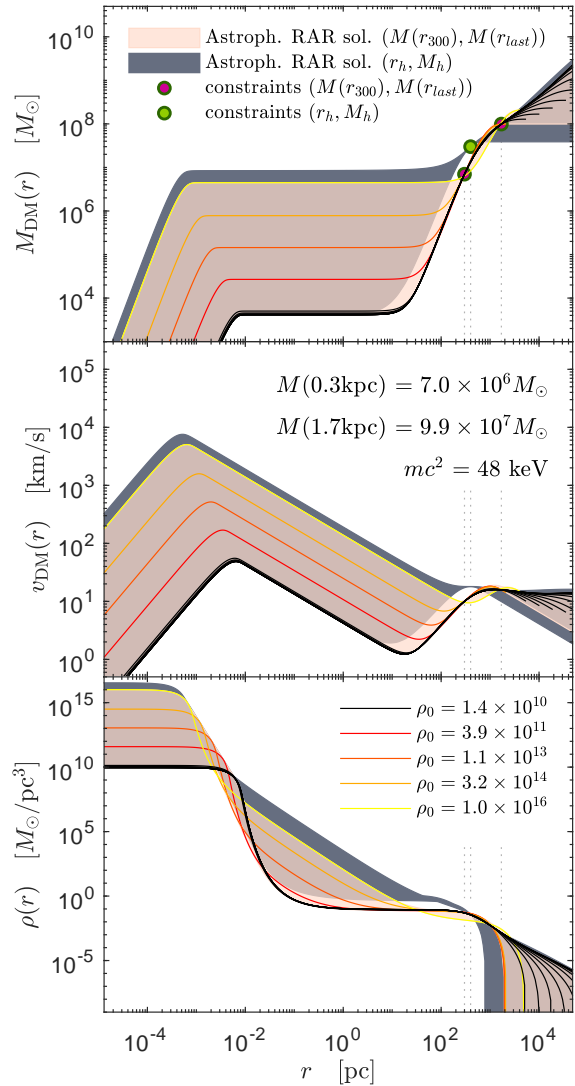


Figure B.9: Comparison between the full window of the astrophysical RAR solutions, as obtained by using the (r_h, M_h) halo constraints (gray shaded regions, coinciding with the bluish region in fig. 1), with those fulfilling the alternative halo constraints ($M(r_{300}), M(r_{\text{last}})$), represented by the light-red shaded regions. The latter belongs to the Fornax dwarf as given in Walker et al. (2009). There is a mild shift in the position of the maximum-circular velocities (roughly a factor 2) between both kind of families (see text for more details). The maximal velocity $v_{\text{max}} \approx 18 \text{ km s}^{-1}$, on the other hand, is exactly obtained in both cases.

well within the 3σ uncertainty area as shown fig. 5. Note that there is an decrease in the plateau density ρ_{pl} of about one order of magnitude but also an increase in the halo radius r_h of about the same order of magnitude. In sum the product $\rho_{\text{pl}}r_h$ remains robust towards a change of constraints.

The main conclusions from the alternative constraints are very similar to conclusions from the halo constraints (r_h, M_h). Thus, we obtain similar effects on the predicted DM magnitudes (such as M_c, M_{tot} and ρ_{pl}) for the differently

DWARFS: FORNAX

$$M(0.3 \text{ kpc}) = 7.0 \times 10^6 M_\odot, M(1.7 \text{ kpc}) = 9.9 \times 10^7 M_\odot$$

ρ_0 M_\odot/pc^3	β_0	θ_0	W_0	M_c M_\odot	r_c pc	M_{tot} M_\odot	r_b pc	ρ_{pl} M_\odot/pc^3
1.4×10^{10}	1.4×10^{-9}	27.4	53.5	4.3×10^3	6.1×10^{-3}	1.3×10^8	5.4×10^3	8.3×10^{-2}
3.9×10^{11}	1.3×10^{-8}	27.5	49.0	2.3×10^4	3.5×10^{-3}	9.9×10^7	2.1×10^3	7.4×10^{-2}
1.1×10^{13}	1.4×10^{-7}	24.6	43.6	1.2×10^5	2.0×10^{-3}	9.9×10^7	2.0×10^3	7.3×10^{-2}
3.2×10^{14}	1.5×10^{-6}	21.4	38.1	6.6×10^5	1.1×10^{-3}	10.0×10^7	2.1×10^3	6.5×10^{-2}
1.0×10^{16}	1.6×10^{-5}	20.2	36.2	3.8×10^6	6.4×10^{-4}	2.1×10^8	4.9×10^3	1.3×10^{-2}

Table B.2: Free RAR model parameters (with $mc^2 = 48 \text{ keV}$) for the 5 benchmark sets of DM profiles, as shown in fig. B.9. They fulfill the observational constraints ($M(0.3 \text{ kpc}) = 7.0 \times 10^6 M_\odot$, $M(1.7 \text{ kpc}) = 9.9 \times 10^7 M_\odot$) for the Fornax dwarf as given in Walker et al. (2009). The characteristic DM masses and radii, given here, have to be compared with those given in table 1 for typical dSphs. Importantly, the predicted M_c , M_{tot} and ρ_{pl} values, by the RAR model in this case, are very similar to the ones obtained for the case of the other halo constraints (r_h , M_h). This indicates the robustness in the RAR predictions.

chosen boundary halo conditions. This maintains intact the main predictions as provided through the halo constraints (r_h , M_h).

Appendix C. The $r_h - M_h$ RAR relation

The aim here is to show that by the usage of the nearly constant DM surface density $\rho_{0\text{D}} r_0 \approx 140 M_\odot \text{pc}^{-2}$ (best-fit) as given in Donato et al. (2009), an approximate (but very useful) relation between the one-halo scale length of the RAR solutions r_h and its mass M_h , is possible (with $\rho_{0\text{D}}$ and r_0 the central DM halo density at the one-halo-scale-length of the Burkert profile). Such (r_h, M_h) relation, obtained without the need to go for specific galaxy-type observables as done in section 3, will be thus applied to cover the gap between dSphs and elliptical galaxies in fig. 6 (represented by the green-ish area).

We start the deduction by recalling the relation between Burkert and RAR one-halo scale lengths $r_0 \approx 2/3 r_h$, as well as the identification $\rho_{0\text{D}} \equiv \rho_{\text{pl}}$, as given in section 5.1. This allows us to write the following new version of the Donato relation

$$\frac{2}{3} \rho_{\text{pl}} r_h = 140 M_\odot / \text{pc}^2 \quad (\text{C.1})$$

Given that typical RAR family solutions develop extended plateaus of nearly constant density all the way up to halo scales, the following approximation holds

$$\rho_{\text{pl}} \approx \frac{3M_h}{4\pi r_h^3} \quad (\text{C.2})$$

The combination of the above two equations directly implies a power law relation $r_h \sim M_h^{0.5}$, which is plotted in fig. C.10, and compared with the somewhat milder power relation followed by the observational constraints (r_h, M_h) obtained in section 3 from dSph to BCGs (in dashed line

joining the coloured dots). The reason why these two relations cannot coincide can be seen through the RAR predictions (vertical thick lines) to the Donato relation in fig. 5, which indeed do not exactly match the Donato best-fit for larger galaxy types. Therefore, an alternative (but equivalent) approach to calculate other families of RAR profiles from new boundary conditions (r_h, M_h) (obtained here from the approximate power law) is possible. Thus, for given halo masses M_h within the range $10^7 - 10^{12} M_\odot$ (and for a fixed surface density $\frac{2}{3} \rho_{\text{pl}} r_h = 140 M_\odot / \text{pc}^2$), one obtains corresponding halo radius r_h , depending on the model parameters. The results cover a regime between dwarfs and ellipticals, shown in the green-ish area in fig. 6, where the white (benchmark) lines (labeled by M_{tot} in the horizontal regime) show the new set of RAR families obtained for those new (r_h, M_h) values. Notice that the continuation of the predicted green-ish area is not extended up to BCGs because the constancy of the DM surface density by Donato et al. (2009) was only provided up to ellipticals.

References

- M. R. Baldeschi, G. B. Gelmini, R. Ruffini, On massive fermions and bosons in galactic halos, *Physics Letters B* 122 (1983) 221–224, doi:10.1016/0370-2693(83)90688-3.
- S.-J. Sin, Late-time phase transition and the galactic halo as a Bose liquid, *Phys. Rev. D* 50 (1994) 3650–3654, doi:10.1103/PhysRevD.50.3650.
- W. Hu, R. Barkana, A. Gruzinov, Fuzzy Cold Dark Matter: The Wave Properties of Ultralight Particles, *Physical Review Letters* 85 (2000) 1158–1161, doi:10.1103/PhysRevLett.85.1158.
- T. Matos, L. Arturo Ureña-López, Further analysis of a cosmological model with quintessence and scalar dark matter, *Phys. Rev. D* 63 (6) 063506, doi:10.1103/PhysRevD.63.063506.
- V. H. Robles, T. Matos, Flat central density profile and constant dark matter surface density in galaxies from scalar field dark matter, *MNRAS* 422 (2012) 282–289, doi:10.1111/j.1365-2966.2012.20603.x.

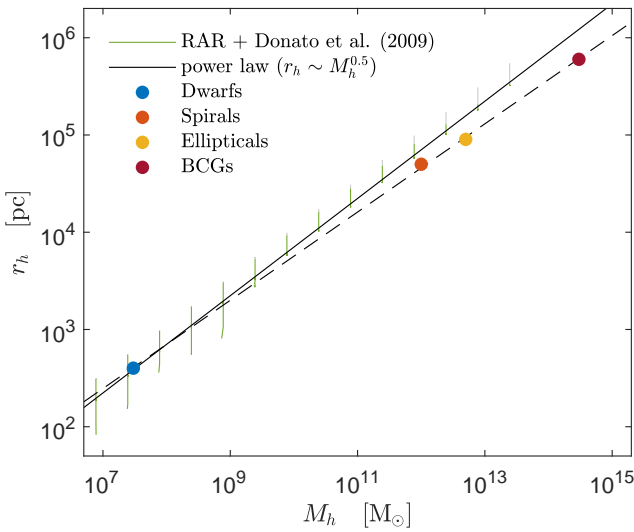


Figure C.10: In dashed (power law) line: correlation between r_h and M_h as inferred from typical galactic structures in section 3, where the coloured points show the typical values of dwarfs, spirals, ellipticals and BCGs. In continuous line: the approximate power law relation $r_h \sim M_h^{0.5}$ as obtained by using the Donato (best-fit) constant value. The vertical dotted lines are RAR predictions for a given halo mass (corresponding with the white curves in fig. 6) for the fixed mean surface density $\frac{2}{3}\rho_{\text{pl}}r_h = 140 M_{\odot}/\text{pc}^2$ given by Donato in Donato et al. (2009).

L. Hui, J. P. Ostriker, S. Tremaine, E. Witten, Ultralight scalars as cosmological dark matter, *Phys. Rev. D* 95 (4) 043541, doi:10.1103/PhysRevD.95.043541.

N. Bar, D. Blas, K. Blum, S. Sibiryakov, Galactic Rotation Curves vs. Ultra-Light Dark Matter: Implications of the Soliton – Host Halo Relation, *ArXiv e-prints*.

C. Destri, H. J. de Vega, N. G. Sanchez, Fermionic warm dark matter produces galaxy cores in the observed scales because of quantum mechanics, *New A* 22 (2013) 39–50, doi:10.1016/j.newast.2012.12.003.

V. Domcke, A. Urbano, Dwarf spheroidal galaxies as degenerate gas of free fermions, *J. Cosmology Astropart. Phys.* 1 002, doi:10.1088/1475-7516/2015/01/002.

L. Randall, J. Scholtz, J. Unwin, Cores in Dwarf Galaxies from Fermi Repulsion, *MNRAS* 467 (2017) 1515–1525, doi:10.1093/mnras/stx161.

H. J. de Vega, P. Salucci, N. G. Sanchez, Observational rotation curves and density profiles versus the Thomas-Fermi galaxy structure theory, *MNRAS* 442 (2014) 2717–2727, doi:10.1093/mnras/stu972.

C. Argüelles, I. Siutsou, R. Ruffini, J. Rueda, B. Machado, On the core-halo constituents of a semi-degenerate gas of massive fermions, in: *Probes of Dark Matter on Galaxy Scales*, 30204, 2013.

C. R. Argüelles, R. Ruffini, Are the most super-massive dark compact objects harbored at the center of dark matter halos?, *International Journal of Modern Physics D* 23 1442020, doi:10.1142/S0218271814420206.

R. Ruffini, C. R. Argüelles, J. A. Rueda, On the core-halo distribution of dark matter in galaxies, *MNRAS* 451 (2015) 622–628, doi:10.1093/mnras/stv1016.

I. Siutsou, C. R. Argüelles, R. Ruffini, Dark matter massive fermions and Einasto profiles in galactic haloes, *Astronomy Reports* 59 (2015) 656–666, doi:10.1134/S1063772915070124.

C. R. Argüelles, N. E. Mavromatos, J. A. Rueda, R. Ruffini, The role of self-interacting right-handed neutrinos in galactic structure, *J. Cosmology Astropart. Phys.* 4 038, doi:10.1088/1475-7516/2016/04/038.

L. G. Gómez, C. R. Argüelles, V. Perlick, J. A. Rueda, R. Ruffini, Strong lensing by fermionic dark matter in galaxies, *Phys. Rev. D* 94 (12) 123004, doi:10.1103/PhysRevD.94.123004.

C. R. Argüelles, A. Krut, J. A. Rueda, R. Ruffini, Novel constraints on fermionic dark matter from galactic observables I: The Milky Way, *Physics of the Dark Universe* 21 (2018) 82–89, doi:10.1016/j.dark.2018.07.002.

H. Deng, M. P. Hertzberg, M. H. Namjoo, A. Masoumi, Can light dark matter solve the core-cusp problem?, *Phys. Rev. D* 98 (2) 023513, doi:10.1103/PhysRevD.98.023513.

F. Donato, G. Gentile, P. Salucci, C. Frigerio Martins, M. I. Wilkinson, G. Gilmore, E. K. Grebel, A. Koch, R. Wyse, A constant dark matter halo surface density in galaxies, *MNRAS* 397 (2009) 1169–1176, doi:10.1111/j.1365-2966.2009.15004.x.

D. C. Rodrigues, A. del Popolo, V. Marra, P. L. C. de Oliveira, Evidence against cuspy dark matter haloes in large galaxies, *MNRAS* 470 (2017) 2410–2426, doi:10.1093/mnras/stx1384.

R. Cen, J. Miralda-Escudé, J. P. Ostriker, M. Rauch, Gravitational collapse of small-scale structure as the origin of the Lyman-alpha forest, *ApJ* 437 (1994) L9–L12, doi:10.1086/187670.

L. Hui, Recovery of the Shape of the Mass Power Spectrum from the Ly α Forest, *ApJ* 516 (1999) 519–526, doi:10.1086/307134.

M. Viel, G. D. Becker, J. S. Bolton, M. G. Haehnelt, Warm dark matter as a solution to the small scale crisis: New constraints from high redshift Lyman- α forest data, *Phys. Rev. D* 88 (4) 043502, doi:10.1103/PhysRevD.88.043502.

C. Yèche, N. Palanque-Delabrouille, J. Baur, H. du Mas des Bourboux, Constraints on neutrino masses from Lyman-alpha forest power spectrum with BOSS and XQ-100, *J. Cosmology Astropart. Phys.* 6 047, doi:10.1088/1475-7516/2017/06/047.

L. Ferrarese, Beyond the Bulge: A Fundamental Relation between Supermassive Black Holes and Dark Matter Halos, *ApJ* 578 (2002) 90–97, doi:10.1086/342308.

J. Kormendy, R. Bender, Supermassive black holes do not correlate with dark matter haloes of galaxies, *Nature* 469 (2011) 377–380, doi:10.1038/nature09695.

Á. Bogdán, A. D. Goulding, Connecting Dark Matter Halos with the Galaxy Center and the Supermassive Black Hole, *ApJ* 800 124, doi:10.1088/0004-637X/800/2/124.

A. Boyarsky, O. Ruchayskiy, D. Iakubovskiy, A. V. Maccio', D. Malyshev, New evidence for dark matter, *ArXiv*: 0911.1774.

P.-H. Chavanis, Generalized thermodynamics and kinetic equations: Boltzmann, Landau, Kramers and Smoluchowski, *Physica A Statistical Mechanics and its Applications* 332 (2004) 89–122, doi:10.1016/j.physa.2003.09.061.

Y. Sofue, Rotation Curve and Mass Distribution in the Galactic Center - From Black Hole to Entire Galaxy, *PASJ* 65 (2013) 118, doi:10.1093/pasj/65.6.118.

M. G. Walker, M. Mateo, E. W. Olszewski, J. Peñarrubia, N. Wyn Evans, G. Gilmore, A Universal Mass Profile for Dwarf Spheroidal Galaxies?, *ApJ* 704 (2009) 1274–1287, doi:10.1088/0004-637X/704/2/1274.

J. S. Bullock, M. Boylan-Kolchin, Small-Scale Challenges to the Λ CDM Paradigm, *ARA&A* 55 (2017) 343–387, doi:10.1146/annurev-astro-091916-055313.

W. J. G. de Blok, F. Walter, E. Brinks, C. Trachternach, S.-H. Oh, R. C. Kennicutt, Jr., High-Resolution Rotation Curves and Galaxy Mass Models from THINGS, *AJ* 136 2648–2719, doi:10.1088/0004-6256/136/6/2648.

H. Hoekstra, B. C. Hsieh, H. K. C. Yee, H. Lin, M. D. Gladders, Virial Masses and the Baryon Fraction in Galaxies, *ApJ* 635 (2005) 73–85, doi:10.1086/496913.

A. J. Romanowsky, C. S. Kochanek, Dynamics of Stars and Globular Clusters in M87, *ApJ* 553 (2001) 722–732, doi:10.1086/320947.

P. E. J. Nulsen, H. Bohringer, A ROSAT determination of the mass of the central Virgo Cluster, *MNRAS* 274 (1995) 1093–1106, doi:10.1093/mnras/274.4.1093.

A. B. Newman, T. Treu, R. S. Ellis, D. J. Sand, The Density Profiles of Massive, Relaxed Galaxy Clusters. II. Separating Luminous and Dark Matter in Cluster Cores, *ApJ* 765 25, doi:10.1088/0004-637X/765/1/25.

- H. Zhao, Analytical models for galactic nuclei, *MNRAS* 278 (1996) 488–496, doi:10.1093/mnras/278.2.488.
- F. Lelli, S. S. McGaugh, J. M. Schombert, SPARC: Mass Models for 175 Disk Galaxies with Spitzer Photometry and Accurate Rotation Curves, *AJ* 152 157, doi:10.3847/0004-6256/152/6/157.
- W. Anderson, Über die Grenzdichte der Materie und der Energie, *Zeitschrift für Physik* 56 (1929) 851–856, doi:10.1007/BF01340146.
- E. Stoner, The Equilibrium of Dense Stars, *The London, Edinburgh, and Dublin Philosophical Magazine and Journal of Science: Series 7, Volume 9, Issue 60, p. 944–963* 9 (1930) 944–963.
- S. Chandrasekhar, The Maximum Mass of Ideal White Dwarfs, *ApJ* 74 (1931a) 81, doi:10.1086/143324.
- S. Chandrasekhar, The highly collapsed configurations of a stellar mass, *MNRAS* 91 (1931b) 456–466, doi:10.1093/mnras/91.5.456.
- L. D. Landau, To the Stars theory, *Phys. Zs. Sowjet.*, vol.1, p.285, 1932 (English and German) 1 (1932) 285.
- J. R. Oppenheimer, G. M. Volkoff, On Massive Neutron Cores, *Physical Review* 55 (1939) 374–381, doi:10.1103/PhysRev.55.374.
- C. E. Rhoades, R. Ruffini, Maximum Mass of a Neutron Star, *Physical Review Letters* 32 (1974) 324–327, doi:10.1103/PhysRevLett.32.324.
- R. V. Wagoner, R. C. Malone, Post-Newtonian Neutron Stars, *ApJ* 189 (1974) L75, doi:10.1086/181468.
- I. Ciufolini, R. Ruffini, On the value of the masses of neutron stars in the parameterized POST Newtonian formalism, *A&A* 97 (1981) L12–L14.
- S. L. Shapiro, S. A. Teukolsky, *Black holes, white dwarfs, and neutron stars: The physics of compact objects*, Wiley, 1983.
- M. Irwin, D. Hatzidimitriou, Structural parameters for the Galactic dwarf spheroidals, *MNRAS* 277 (1995) 1354–1378, doi:10.1093/mnras/277.4.1354.
- I. D. Karachentsev, V. E. Karachentseva, W. K. Huchtmeier, D. I. Makarov, A Catalog of Neighboring Galaxies, *AJ* 127 (2004) 2031–2068, doi:10.1086/382905.
- J. D. Wing, E. L. Blanton, An Examination of the Optical Substructure of Galaxy Clusters Hosting Radio Sources, *ApJ* 767 102, doi:10.1088/0004-637X/767/2/102.
- A. C. Seth, R. van den Bosch, S. Mieske, H. Baumgardt, M. D. Brok, J. Strader, N. Neumayer, I. Chilingarian, M. Hilker, R. McDermid, L. Spitler, J. Brodie, M. J. Frank, J. L. Walsh, A supermassive black hole in an ultra-compact dwarf galaxy, *Nature* 513 (2014) 398–400, doi:10.1038/nature13762.
- C. P. Ahn, A. C. Seth, M. den Brok, J. Strader, H. Baumgardt, R. van den Bosch, I. Chilingarian, M. Frank, M. Hilker, R. McDermid, S. Mieske, A. J. Romanowsky, L. Spitler, J. Brodie, N. Neumayer, J. L. Walsh, Detection of Supermassive Black Holes in Two Virgo Ultracompact Dwarf Galaxies, *ApJ* 839 72, doi:10.3847/1538-4357/aa6972.
- C. P. Ahn, A. C. Seth, M. Cappellari, D. Krajnović, J. Strader, K. T. Voggel, J. L. Walsh, A. Bahramian, H. Baumgardt, J. Brodie, I. Chilingarian, L. Chomiuk, M. den Brok, M. Frank, M. Hilker, R. M. McDermid, S. Mieske, N. Neumayer, D. D. Nguyen, R. Pechetti, A. J. Romanowsky, L. Spitler, The Black Hole in the Most Massive Ultracompact Dwarf Galaxy M59-UCD3, *ApJ* 858 102, doi:10.3847/1538-4357/aabc57.
- A. V. Afanasiev, I. V. Chilingarian, S. Mieske, K. T. Voggel, A. Picotti, M. Hilker, A. Seth, N. Neumayer, M. Frank, A. J. Romanowsky, G. Hau, H. Baumgardt, C. Ahn, J. Strader, M. den Brok, R. McDermid, L. Spitler, J. Brodie, J. L. Walsh, A 3.5 million Solar masses black hole in the centre of the ultracompact dwarf galaxy fornax UCD3, *MNRAS* 477 (2018) 4856–4865, doi:10.1093/mnras/sty913.
- B. Kızıltan, H. Baumgardt, A. Loeb, An intermediate-mass black hole in the centre of the globular cluster 47 Tucanae, *Nature* 542 (2017) 203–205, doi:10.1038/nature21361.
- B. B. P. Perera, B. W. Stappers, A. G. Lyne, C. G. Bassa, I. Cognard, L. Guillemot, M. Kramer, G. Theureau, G. Desvignes, Evidence for an intermediate-mass black hole in the globular cluster NGC 6624, *MNRAS* 468 (2017) 2114–2127, doi:10.1093/mnras/stx501.
- L. Ferrarese, D. Merritt, A Fundamental Relation between Supermassive Black Holes and Their Host Galaxies, *ApJ* 539 (2000) L9–L12, doi:10.1086/312838.
- K. Gebhardt, R. Bender, G. Bower, A. Dressler, S. M. Faber, A. V. Filippenko, R. Green, C. Grillmair, L. C. Ho, J. Kormendy, T. R. Lauer, J. Magorrian, J. Pinkney, D. Richstone, S. Tremaine, A Relationship between Nuclear Black Hole Mass and Galaxy Velocity Dispersion, *ApJ* 539 (2000) L13–L16, doi:10.1086/312840.
- K. Gültekin, D. O. Richstone, K. Gebhardt, T. R. Lauer, S. Tremaine, M. C. Aller, R. Bender, A. Dressler, S. M. Faber, A. V. Filippenko, R. Green, L. C. Ho, J. Kormendy, J. Magorrian, J. Pinkney, C. Siopis, The M- σ and M-L Relations in Galactic Bulges, and Determinations of Their Intrinsic Scatter, *ApJ* 698 (2009) 198–221, doi:10.1088/0004-637X/698/1/198.
- M. Valluri, L. Ferrarese, D. Merritt, C. L. Joseph, The Low End of the Supermassive Black Hole Mass Function: Constraining the Mass of a Nuclear Black Hole in NGC 205 via Stellar Kinematics, *ApJ* 628 (2005) 137–152, doi:10.1086/430752.
- J. E. Greene, C. Y. Peng, M. Kim, C.-Y. Kuo, J. A. Braatz, C. M. V. Impellizzeri, J. J. Condon, K. Y. Lo, C. Henkel, M. J. Reid, Precise Black Hole Masses from Megamaser Disks: Black Hole-Bulge Relations at Low Mass, *ApJ* 721 (2010) 26–45, doi:10.1088/0004-637X/721/1/26.
- D. J. E. Marsh, J. Silk, A model for halo formation with axion mixed dark matter, *MNRAS* 437 (2014) 2652–2663, doi:10.1093/mnras/stt2079.
- E. Armengaud, N. Palanque-Delabrouille, C. Yèche, D. J. E. Marsh, J. Baur, Constraining the mass of light bosonic dark matter using SDSS Lyman- α forest, *MNRAS* 471 (2017) 4606–4614, doi:10.1093/mnras/stx1870.
- P.-H. Chavanis, M. Lemou, F. Méhats, Models of dark matter halos based on statistical mechanics: The fermionic King model, *Phys. Rev. D* 92 (12) 123527, doi:10.1103/PhysRevD.92.123527.
- L. E. Strigari, J. S. Bullock, M. Kaplinghat, J. D. Simon, M. Geha, B. Willman, M. G. Walker, A common mass scale for satellite galaxies of the Milky Way, *Nature* 454 (2008) 1096–1097, doi:10.1038/nature07222.